Chapter 8

Analyzing Wave Propagation in Helical Waveguides Using Laplace, Fourier, and Their Inverse Transforms, and Applications

Z. Menachem and S. Tapuchi

Additional information is available at the end of the chapter

http://dx.doi.org/10.5772/50020

1. Introduction

Various methods for the analysis of wave propagation in the curved waveguides have been studied in the literature. Two interesting methods of investigation of propagation along the curved waveguides are based on the ray model and the mode model. A review of the hollow waveguide technology [1-2] and a review of IR transmitting, hollow waveguides, fibers and integrated optics [3] were published. The first theoretical analysis of the problem of hollow cylindrical bent waveguides was published by Marcatili and Schmeltzer [4], where the theory considers the bending as a small disturbance and uses cylindrical coordinates to solve Maxwell equations. They derive the mode equations of the disturbed waveguide using the ratio of the inner radius r to the curvature radius R as a small parameter ($r/R \ll 1$). Their theory predicts that the bending has little influence on the attenuation of a hollow metallic waveguide. Marhic [5] proposed a mode-coupling analysis of the bending losses of circular metallic waveguide in the IR range for large bending radii. In the circular guide it is found that the preferred TE_{01} mode can couple very effectively to the lossier TM_{11} mode when the guide undergoes a circular bend. For circular waveguides, the microwave approximation has been used for the index of refraction and the straight guide losses, and the results indicate very poor bending properties due to the near degeneracy of the TE_{01} and TM_{11} modes, thereby offering an explanation for the high losses observed in practice.

Miyagi et al. [6] suggested an improved solution, which provided agreement with the experimental results, but only for $r/R \ll 1$. A different approach [5,7] treats the bending as a perturbation that couples the modes of a straight waveguide. That theory explains the large difference between the metallic and metallic-dielectric bent waveguide attenuation. The reason for this difference is that in metallic waveguides the coupling between the TE and TM modes caused by the bending mixes modes with very low attenuation and modes with very high attenuation, whereas in metallic-dielectric waveguides, both the TE and TM

modes have low attenuation. Hollow waveguides with both metallic and dielectric internal layers were proposed to reduce the transmission losses. Hollow-core waveguides have two possibilities. The inner core materials have relative refractive indices greater than one (namely, leaky waveguides) or the inner wall material has a relative refractive index of less than one. A hollow waveguide can be made, in principle, from any flexible or rigid tube (plastic, glass, metal, etc.) if its inner hollow surface (the core) is covered by a metallic layer and a dielectric overlayer. This layer structure enables us to transmit both the TE and TM polarization with low attenuation [5,7].

A method for the electromagnetic (EM) analysis of bent waveguides [8] is based on the expansion of the bend mode in modes of the straight waveguides, including the modes under the cutoff. A different approach to calculate the bending losses in curved dielectric waveguides [9] is based on the well-known conformal transformation of the index profile and on vectorial eigenmode expansion combined with perfectly matched layer boundary conditions to accurately model radiation losses. An improved ray model for simulating the transmission of laser radiation through a metallic or metallic dielectric multibent hollow cylindrical waveguide was proposed [10-11]. It was shown theoretically and proved experimentally that the transmission of CO_2 laser radiation is possible even through bent waveguide.

The propagation of EM waves in a loss-free inhomogeneous hollow conducting waveguide with a circular cross section and uniform plane curvature of the longitudinal axis was considered [12]. For small curvature the field equations can be solved by means of an analytical approximation method. In this approximation the curvature of the axis of the waveguide was considered as a disturbance of the straight circular cylinder, and the perturbed torus field was expanded in eigenfunctions of the unperturbed problem. An extensive survey of the related literature can be found especially in the book on EM waves and curved structures [13]. The radiation from curved open structures is mainly considered by using a perturbation approach, that is by treating the curvature as a small perturbation of the straight configuration. The perturbative approach is not entirely suitable for the analysis of relatively sharp bends, such as those required in integrated optics and especially short millimeter waves. The models based on the perturbation theory consider the bending as a perturbation ($r/R \ll 1$), and solve problems only for a large radius of curvature.

Several methods of investigation of propagation were developed for study of empty curved waveguide and bends [14-17]. The results of precise numerical computations and extensive analytical investigation of the angular propagation constants were presented for various electromagnetic modes which may exit in waveguide bends of rectangular cross section [14]. A new equivalent circuit for circular E-plane bends, suitable for any curvature radius and rectangular waveguide type was presented in Ref. [15]. An accurate and efficient method of moments solution together with a mode-matching technique for the analysis of curved bends in a general parallel-plate waveguide was described in the case of a rectangular waveguides [16]. A rigorous differential method describing the propagation of an electromagnetic wave in a bent waveguide was presented in Ref. [17].

Several methods of propagation along the toroidal and helical waveguides were developed, based on Maxwell's equations. The method for the analysis of EM wave propagation along

the toroidal waveguide [18] has been derived with arbitrary profiles, and with rectangular metal tubes. An improved approach has been derived for the propagation of EM field along a toroidal dielectric waveguide with a circular cross-section [19]. The meaning of the improved approach is that the method employs helical coordinates (and not cylindrical coordinate, such as in the methods that considered the bending as a perturbation). Thus the Laplacian of the wave equations is based on the metric coefficients in the case of the helical waveguide with a circular cross section. The method for the propagation of EM field along a helical dielectric waveguide with a circular cross section [20] has been proposed. The method for the propagation of EM field along a helical dielectric waveguide with a rectangular cross section has been proposed [21]. It is very interesting to compare between the mode model methods for wave propagation in the curved waveguide with a rectangular cross section and with a circular cross section. The methods [18-19] have been derived for one bending of the toroidal waveguide (approximately a plane curve) in the case of small values of step angle of the helix. The methods [20-21] have been derived for one bending of the helical waveguide (a space curved waveguide) for an arbitrary value of the step's angle of the helix. These methods were generalized from a toroidal dielectric waveguide (approximately a plane curve) with one bending to a helical waveguide (a space curved waveguide for an arbitrary value of the step's angle of the helix) with one bending. The two above methods employ toroidal or helical coordinates (and not cylindrical coordinates, such as in the methods that considered the bending as a perturbation ($r/R \ll 1$)), and the calculations are based on using Laplace and Fourier transforms, and the output fields are computed by the inverse Laplace and Fourier transforms. Laplace transform on the differential wave equations is needed to obtain the wave equations (and thus also the output fields) that are expressed directly as functions of the transmitted fields at the entrance of the waveguide at $\zeta = 0^+$. Thus, the Laplace transform is necessary to obtain the comfortable and simple *input-output* connections of the fields.

This chapter presents two improved methods for the propagation of EM fields along a helical dielectric waveguide with a circular cross section and a rectangular cross section. The two different methods employ helical coordinates (and not cylindrical coordinates, such as in the methods that considered the bending as a perturbation). The calculations are based on using Laplace and Fourier transforms, and the output fields are computed by the inverse Laplace and Fourier transforms. Laplace transform on the differential wave equations is needed to obtain the wave equations and the output fields that are expressed directly as functions of the transmitted fields at the entrance of the waveguide. Thus, the Laplace transform is necessary to obtain the comfortable and simple *input-output* connections of the fields. The output power transmission and the output power density are improved by increasing the step's angle or the radius of the cylinder of the helix, especially in the cases of space curved waveguides. These methods can be a useful tool to improve the output results in all the cases of the hollow helical waveguides in medical and industrial regimes (by the first method) and in the microwave and millimeter-wave regimes, for the diffused optical waveguides in integrated optics (by the second method).

2. The derivation of the two different methods

This chapter presents two improved methods for the propagation of EM fields along a helical dielectric waveguide with a circular cross section (by the first method) and a rectangular

cross section (by the second method). A general scheme of the helical coordinate system (r, θ, ζ) is shown in Fig. 1(a) and the circular helical waveguide is shown in Fig. 1(b), where $0 \leq r \leq a + \delta_m$, and 2a is the internal diameter of the cross-section. A general scheme of the helical coordinate system (x, y, ζ) is shown in Fig. 1(c) and the rectangular helical waveguide is shown in Fig. 1(d), where $0 \leq x \leq a$, $0 \leq y \leq b$, and a and b are the dimensions in the cross section. In these figures, R is the radius of the cylinder, and ζ is the coordinate along the axis of the helical waveguide.

It is very interesting to compare between the mode model methods for wave propagation in the helical waveguide with a circular cross section and in the helical waveguide with a rectangular cross section. These the two kinds of the different methods enable us to solve practical problems with different boundary conditions. The two methods employ helical coordinates (and not cylindrical coordinates, such as in the methods that considered the bending as a perturbation (r/R)). The calculations are based on using Laplace and Fourier transforms, and the output fields are computed by the inverse Laplace and Fourier transforms. Laplace transform on the differential wave equations is needed to obtain the wave equations (and thus also the output fields) that are expressed directly as functions of the transmitted fields at the entrance of the waveguide at $\zeta = 0^+$. Thus, the Laplace transform is necessary to obtain the comfortable and simple *input-output* connections of the fields. The derivation for a helical waveguide with a circular cross section is given in detail in [20]. The derivation for a helical waveguide with a rectangular cross section is given in detail in [21]. Let us repeat these difference methods, in brief.

2.1 Formulation of the problem for the helical coordinate system (r, θ, ζ) and for the helical coordinate system (x, y, ζ).

We start by finding the metric coefficients from the helical transformation of the coordinates. The helical transformation of the coordinates is achieved by two rotations and one translation, and is given in the form:

$$\begin{pmatrix} X \\ Y \\ Z \end{pmatrix} = \begin{pmatrix} cos(\phi_c) & -sin(\phi_c) & 0 \\ sin(\phi_c) & cos(\phi_c) & 0 \\ 0 & 0 & 1 \end{pmatrix} \begin{pmatrix} 1 & 0 & 0 \\ 0 & cos(\delta_p) & -sin(\delta_p) \\ 0 & sin(\delta_p) & cos(\delta_p) \end{pmatrix} \begin{pmatrix} r\sin\theta \\ 0 \\ r\cos\theta \end{pmatrix} + \begin{pmatrix} Rcos(\phi_c) \\ Rsin(\phi_c) \\ \zeta sin(\delta_p) \end{pmatrix}, \quad (1)$$

where ζ is the coordinate along the helix axis, R is the radius of the cylinder, δ_p is the step's angle of the helix (see Figs. (2(a))-(2(b))), and $\phi_c = (\zeta\cos(\delta_p))/R$. Likewise, $0 \leq r \leq a + \delta_m$, where 2a is the internal diameter of the cross-section of the helical waveguide, and δ_m is the thickness of the metallic layer, as shown in Fig. 3(a).

Figure 2(a) shows the rotations and translation of the orthogonal system ($\overline{X}$, $\overline{\zeta}$, $\overline{Z}$) from point *A* to the orthogonal system (X,Y,Z) at point *K*. Figure 2(b) shows the deployment of the helix depicted in Fig. 2(a).

According to Equation (1), the helical transformation of the coordinates with a circular cross section becomes

$$X = (R + r\sin\theta)\cos(\phi_c) + r\sin(\delta_p)\cos\theta\sin(\phi_c), \quad (2a)$$

$$Y = (R + r\sin\theta)\sin(\phi_c) - r\sin(\delta_p)\cos\theta\cos(\phi_c), \quad (2b)$$

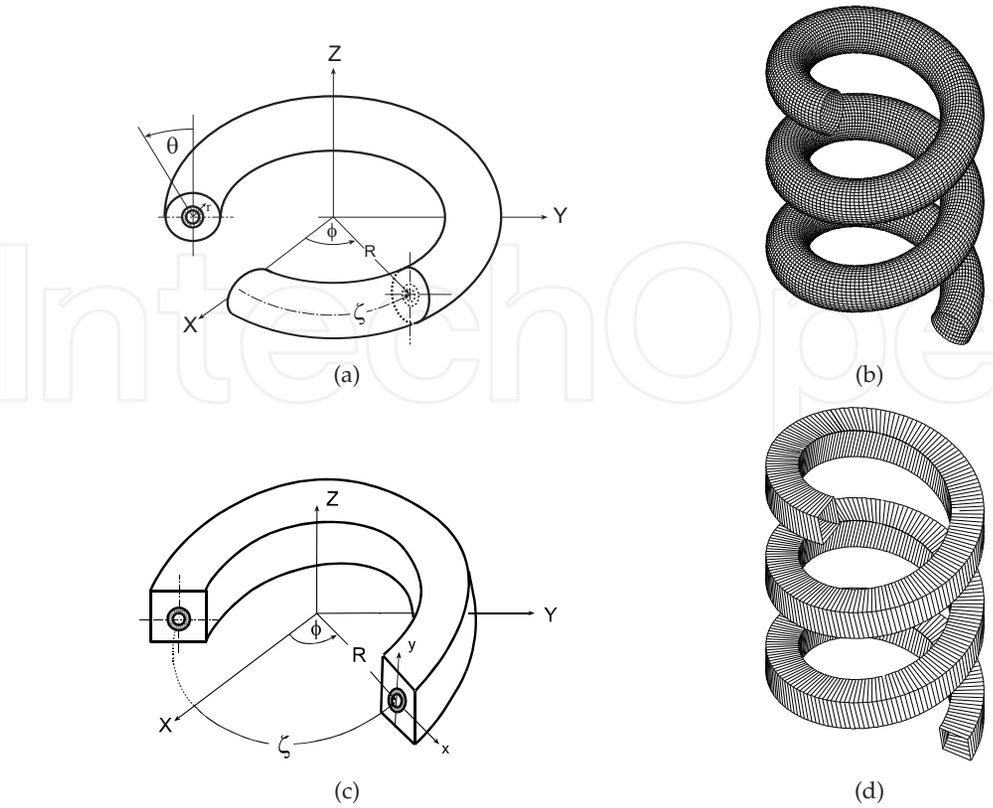

Figure 1. (a) A general scheme of the helical coordinate system (r, θ, ζ). (b) The circular helical waveguide. (c) A general scheme of the helical coordinate system (x, y, ζ). (d) The rectangular helical waveguide.

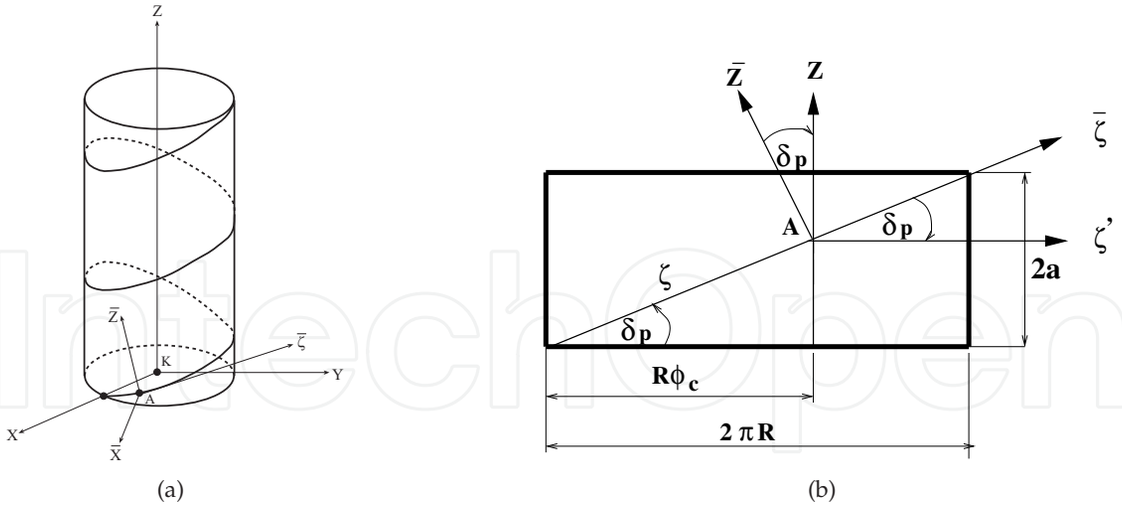

(a) (b)

Figure 2. (a) Rotations and translation of the orthogonal system ($\overline{X}$, $\overline{\zeta}$, $\overline{Z}$) from point A to the orthogonal system (X,Y,Z) at point K. (b) Deployment of the helix.

$$Z = r\cos\theta\cos(\delta_p) + \zeta\sin(\delta_p), \tag{2c}$$

where $\phi_c = (\zeta/R)\cos(\delta_p)$, R is the radius of the cylinder, and (r, θ) are the parameters of the cross-section. Note that $\zeta\sin(\delta_p) = R\phi_c\tan(\delta_p)$.

The metric coefficients in the case of the helical waveguide with a circular cross section, according to Eqs. (2a)-(2c) are:

$$h_r = 1, \tag{3a}$$

$$h_\theta = r, \tag{3b}$$

$$h_\zeta = \sqrt{\left(1+\frac{r}{R}\sin\theta\right)^2\cos^2(\delta_p)+\sin^2(\delta_p)\left(1+\frac{r^2}{R^2}\cos^2\theta\cos^2(\delta_p)\right)}$$

$$= \sqrt{1+\frac{2r}{R}\sin\theta\cos^2(\delta_p)+\frac{r^2}{R^2}\sin^2\theta\cos^2(\delta_p)+\frac{r^2}{R^2}\cos^2\theta\cos^2(\delta_p)\sin^2(\delta_p)}$$

$$\simeq 1+\frac{r}{R}\sin\theta\cos^2(\delta_p). \tag{3c}$$

Note that the third and the fourth terms in the root of the metric coefficient h_ζ are negligible in comparison to the first and the second terms when $(r/R)^2 \ll 1$.

The metric coefficients, and the helical transformation in the case of the helical coordinate system (x, y, ζ) are given from the above equations for the helical coordinate system (r, θ, ζ) and according to Fig. 1(a), where $r\sin\theta = x$, and $r\cos\theta = y$. Thus, the metric coefficients in the case of the helical waveguide with a rectangular cross section are:

$$h_x = 1, \tag{4a}$$

$$h_y = 1, \tag{4b}$$

$$h_\zeta \simeq 1+\frac{x}{R}\cos^2(\delta_p). \tag{4c}$$

3. Solution of the wave equations for the helical coordinate system (r, θ, ζ) and for the helical coordinate system (x, y, ζ).

The two kinds of the different methods enable us to solve practical problems with different boundary conditions. The two methods employ helical coordinates (and not cylindrical coordinates, such as in the methods that considered the bending as a perturbation (r/R $\ll$ 1)). The calculations are based on using Laplace and Fourier transforms, and the output fields are computed by the inverse Laplace and Fourier transforms. Laplace transform on the differential wave equations is needed to obtain the wave equations (and thus also the output fields) that are expressed directly as functions of the transmitted fields at the entrance of the waveguide at $\zeta = 0^+$. Thus, the Laplace transform is necessary to obtain the comfortable and simple *input-output* connections of the fields.

3.1 Solution of the wave equations for the helical coordinate system (r, θ, ζ).

The derivation is based on an arbitrary value of the step's angle of the helix (δ_p). The derivation is based on Maxwell's equations for the computation of the EM field and the radiation power density at each point during propagation along a helical waveguide, with a radial dielectric profile. The longitudinal components of the fields are developed into the

Fourier-Bessel series. The transverse components of the fields are expressed as a function of the longitudinal components in the Laplace transform domain. Finally, the transverse components of the fields are obtained by using the inverse Laplace transform by the residue method, for an arbitrary value of the step's angle of the helix (δ_p).

The derivation is given for the lossless case to simplify the mathematical expressions. In a linear lossy medium, the solution is obtained by replacing the permitivity ϵ by $\epsilon_c = \epsilon - j(\sigma/\omega)$ in the solutions for the lossless case, where ϵ_c is the complex dielectric constant, and σ is the conductivity of the medium. The boundary conditions for a lossy medium are given after the derivation. For most materials, the permeability μ is equal to that of free space ($\mu = \mu_0$). The wave equations for the electric and magnetic field components in the inhomogeneous dielectric medium $\epsilon(r)$ are given by

$$\nabla^2 \boldsymbol{E} + \omega^2 \mu \epsilon \boldsymbol{E} + \nabla \left(\boldsymbol{E} \cdot \frac{\nabla \epsilon}{\epsilon} \right) = 0, \tag{5a}$$

and

$$\nabla^2 \boldsymbol{H} + \omega^2 \mu \epsilon \boldsymbol{H} + \frac{\nabla \epsilon}{\epsilon} \times (\nabla \times \boldsymbol{H}) = 0, \tag{5b}$$

respectively. The transverse dielectric profile ($\epsilon(r)$) is defined as $\epsilon_0(1 + g(r))$, where ϵ_0 represents the vacuum dielectric constant, and $g(r)$ is its profile function in the waveguide. The normalized transverse derivative of the dielectric profile (g_r) is defined as $(1/\epsilon(r))(\partial\epsilon(r)/\partial r)$.

From the transformation of Eqs. (3a)-(3c) we can derive the Laplacian of the vector $\boldsymbol{E}$ (i.e., $\nabla^2\boldsymbol{E}$), and obtain the wave equations for the electric and magnetic fields in the inhomogeneous dielectric medium. It is necessary to find the values of $\nabla \cdot \boldsymbol{E}$, $\nabla(\nabla \cdot \boldsymbol{E})$, $\nabla \times \boldsymbol{E}$, and $\nabla \times (\nabla \times \boldsymbol{E})$ in order to obtain the value of $\nabla^2\boldsymbol{E}$, where $\nabla^2\boldsymbol{E} = \nabla(\nabla \cdot \boldsymbol{E}) - \nabla \times (\nabla \times \boldsymbol{E})$. All these values are dependent on the metric coefficients (3a,b,c).

The ζ component of $\nabla^2\boldsymbol{E}$ is given by

$$(\nabla^2 \boldsymbol{E})_\zeta = \nabla^2 E_\zeta + \frac{2}{R h_\zeta^2} \left[\sin\theta \frac{\partial}{\partial \zeta} E_r + \cos\theta \frac{\partial}{\partial \zeta} E_\theta \right] - \frac{1}{R^2 h_\zeta^2} E_\zeta, \tag{6}$$

where

$$\nabla^2 E_\zeta = \frac{\partial^2}{\partial r^2} E_\zeta + \frac{1}{r^2} \frac{\partial^2}{\partial \theta^2} E_\zeta + \frac{1}{r} \frac{\partial}{\partial r} E_\zeta + \frac{1}{h_\zeta} \left[\frac{\sin\theta}{R} \frac{\partial}{\partial r} E_\zeta + \frac{\cos\theta}{rR} \frac{\partial}{\partial \theta} E_\zeta + \frac{1}{h_\zeta} \frac{\partial^2}{\partial \zeta^2} E_\zeta \right], \tag{7}$$

and in the case of $h_\zeta = 1 + (r/R)\sin\theta\cos^2(\delta_p)$.

The longitudinal components of the wave equations (5a) and (5b) are obtained by deriving the following terms

$$\left[\nabla \left(\boldsymbol{E} \cdot \frac{\nabla \epsilon}{\epsilon} \right) \right]_\zeta = \frac{1}{h_\zeta} \frac{\partial}{\partial \zeta} \left[E_r g_r \right], \tag{8}$$

and

$$\left[\frac{\nabla\epsilon}{\epsilon}\times(\nabla\times\boldsymbol{H})\right]_{\zeta}=j\omega\epsilon\left[\frac{\nabla\epsilon}{\epsilon}\times\boldsymbol{E}\right]_{\zeta}=j\omega\epsilon g_r E_\theta. \tag{9}$$

The longitudinal components of the wave equations (5a) and (5b) are then written in the form

$$\left(\nabla^2\boldsymbol{E}\right)_{\zeta}+k^2E_\zeta+\frac{1}{h_\zeta}\frac{\partial}{\partial\zeta}\left(E_r g_r\right)=0, \tag{10}$$

$$\left(\nabla^2\boldsymbol{H}\right)_{\zeta}+k^2H_\zeta+j\omega\epsilon g_r E_\theta=0, \tag{11}$$

where $(\nabla^2\mathbf{E})_\zeta$, for instance, is given in Eq. (6). The *local* wave number parameter is $k=\omega\sqrt{\mu\epsilon(r)}=k_0\sqrt{1+g(r)}$, where the free-space wave number is $k_0=\omega\sqrt{\mu_0\epsilon_0}$.

The transverse Laplacian operator is defined as

$$\nabla_\perp^2\equiv\nabla^2-\frac{1}{h_\zeta^2}\frac{\partial^2}{\partial\zeta^2}. \tag{12}$$

The Laplace transform

$$\tilde{a}(s)=\mathcal{L}\{a(\zeta)\}=\int_{\zeta=0}^{\infty}a(\zeta)e^{-s\zeta}d\zeta \tag{13}$$

is applied on the ζ-dimension, where $a(\zeta)$ represents any ζ-dependent variables, where $\zeta=(R\phi_c)/\cos(\delta_p)$.

The next four steps are given in detail in Ref. [19], as a part of our derivation. Let us repeat these four steps, in brief.

1). By substituting Eq.(6) into Eq.(10) and by using the Laplace transform (13), the longitudinal components of the wave equations (Eqs. (10)-(11)) are described in the Laplace transform domain, as *coupled* wave equations.

2). The transverse fields are obtained directly from Maxwell's equations, and by using the Laplace transform (13), and are given by

$$\tilde{E}_r(s)=\frac{1}{s^2+k^2h_\zeta^2}\left\{-\frac{j\omega\mu_0}{r}\left[\frac{r}{R}\cos\theta\cos^2(\delta_p)\tilde{H}_\zeta+h_\zeta\frac{\partial}{\partial\theta}\tilde{H}_\zeta\right]h_\zeta+s\left[\frac{\sin\theta}{R}\cos^2(\delta_p)\tilde{E}_\zeta+h_\zeta\frac{\partial}{\partial r}\tilde{E}_\zeta\right]\right.$$

$$\left.+sE_{r_0}-j\omega\mu_0H_{\theta_0}h_\zeta\right\}, \tag{14a}$$

$$\tilde{E}_\theta(s)=\frac{1}{s^2+k^2h_\zeta^2}\left\{\frac{s}{r}\left[\frac{r}{R}\cos\theta\cos^2(\delta_p)\tilde{E}_\zeta+h_\zeta\frac{\partial}{\partial\theta}\tilde{E}_\zeta\right]+j\omega\mu_0h_\zeta\left[\frac{\sin\theta}{R}\cos^2(\delta_p)\tilde{H}_\zeta+h_\zeta\frac{\partial}{\partial r}\tilde{H}_\zeta\right]\right.$$

$$\left.+sE_{\theta_0}+j\omega\mu_0H_{r_0}h_\zeta\right\}, \tag{14b}$$

$$\tilde{H}_r(s) = \frac{1}{s^2 + k^2 h_\zeta^2}\left\{ \frac{j\omega\epsilon}{r}\left[\frac{r}{R}\cos\theta\cos^2(\delta_p)\tilde{E}_\zeta + h_\zeta\frac{\partial}{\partial\theta}\tilde{E}_\zeta\right]h_\zeta + s\left[\frac{\sin\theta}{R}\cos^2(\delta_p)\tilde{H}_\zeta + h_\zeta\frac{\partial}{\partial r}\tilde{H}_\zeta\right] + sH_{r_0} + j\omega\epsilon E_{\theta_0}h_\zeta\right\}, \tag{14c}$$

$$\tilde{H}_\theta(s) = \frac{1}{s^2 + k^2 h_\zeta^2}\left\{ \frac{s}{r}\left[\frac{r}{R}\cos\theta\cos^2(\delta_p)\tilde{H}_\zeta + h_\zeta\frac{\partial}{\partial\theta}\tilde{H}_\zeta\right] - j\omega\epsilon h_\zeta\left[\frac{\sin\theta}{R}\cos^2(\delta_p)\tilde{E}_\zeta + h_\zeta\frac{\partial}{\partial r}\tilde{E}_\zeta\right] + sH_{\theta_0} - j\omega\epsilon E_{r_0}h_\zeta\right\}. \tag{14d}$$

Note that the transverse fields are dependent only on the longitudinal components of the fields and as function of the step's angle (δ_p) of the helix.

3). The transverse fields are substituted into the *coupled* wave equations.

4). The longitudinal components of the fields are developed into Fourier-Bessel series, in order to satisfy the metallic boundary conditions of the circular cross-section. The condition is that we have only ideal boundary conditions for r=a. Thus, the electric and magnetic fields will be zero in the metal.

5). Two sets of equations are obtained by substitution the longitudinal components of the fields into the wave equations. The first set of the equations is multiplied by $\cos(n\theta)J_n(P_{nm}r/a)$, and after that by $\sin(n\theta)J_n(P_{nm}r/a)$, for $n \neq 0$. Similarly, the second set of the equations is multiplied by $\cos(n\theta)J_n(P^{'}{}_{nm}r/a)$, and after that by $\sin(n\theta)J_n(P^{'}{}_{nm}r/a)$, for $n \neq 0$.

6). In order to find an algebraic system of four equations with four unknowns, it is necessary to integrate over the area (r,θ), where $r = [0,a]$, and $\theta = [0,2\pi]$, by using the orthogonal-relations of the trigonometric functions.

7). The propagation constants β_{nm} and $\beta^{'}_{nm}$ of the TM and TE modes of the hollow waveguide [22] are given, respectively, by $\beta_{nm} = \sqrt{k_o^2 - (P_{nm}/a)^2}$ and $\beta^{'}_{nm} = \sqrt{k_o^2 - (P^{'}_{nm}/a)^2}$, where the transverse Laplacian operator ($\nabla_\perp^2$) is given by $-(P_{nm}/a)^2$ and $-(P^{'}_{nm}/a)^2$ for the TM and TE modes of the hollow waveguide, respectively.

The separation of variables is obtained by using the preceding orthogonal-relations. Thus the algebraic equations (n $\neq$ 0) are given by

$$\alpha_n{}^{(1)}A_n + \beta_n{}^{(1)}D_n = \frac{1}{\pi}\widehat{(BC1)}_n, \tag{15a}$$

$$\alpha_n{}^{(2)}B_n + \beta_n{}^{(2)}C_n = \frac{1}{\pi}\widehat{(BC2)}_n, \tag{15b}$$

$$\beta_n{}^{(3)}B_n + \alpha_n{}^{(3)}C_n = \frac{1}{\pi}\widehat{(BC3)}_n, \tag{15c}$$

$$\beta_n{}^{(4)}A_n + \alpha_n{}^{(4)}D_n = \frac{1}{\pi}\widehat{(BC4)}_n. \tag{15d}$$

Further we assume $n^{'}$=n=1. The elements (${\alpha_n}^{(1)}$, ${\beta_n}^{(1)}$, etc), on the left side of (15a) for n=1 are given for an arbitrary value of the step's angle (δ_p) by:

$$
\begin{aligned}
{\alpha_1}^{(1)mm'} &= \pi\left(s^2+\beta_{1m'}^2\right)\left[\left(s^2+{k_0}^2\right)G_{00}^{(1)mm'}+{k_0}^2G_{01}^{(1)mm'}\right] \\
&+\pi\frac{1}{R^4}{k_0}^2s^2\left(\frac{1}{4}\cos^4(\delta_p)G_{02}^{(1)mm'}+\frac{1}{2}\cos^4(\delta_p)G_{03}^{(1)mm'}\right) \\
&+\pi{k_0}^2\Bigg\{s^2G_{01}^{(1)mm'}+G_{05}^{(1)mm'}+\frac{1}{R^2}\left(G_{00}^{(1)mm'}+G_{01}^{(1)mm'}\right)+\frac{3}{2R^2}\beta_{1m'}^2\cos^4(\delta_p)\left(G_{02}^{(1)mm'}+G_{03}^{(1)mm'}\right) \\
&+\frac{1}{4R^4}\cos^4(\delta_p)\left(G_{02}^{(1)mm'}+G_{03}^{(1)mm'}\right)+\frac{1}{8R^4}\cos^8(\delta_p)\left(G_{06}^{(1)mm'}+G_{07}^{(1)mm'}\right)\Bigg\} \\
&+\pi s^2\Bigg[G_{08}^{(1)mm'}+\frac{1}{2R^2}\cos^2(\delta_p)G_{00}^{(1)mm'}+\frac{1}{4R^2}\left(\cos^4(\delta_p)\beta_{1m'}^2G_{02}^{(1)mm'}+\cos^2(\delta_p)G_{09}^{(1)mm'}\right) \\
&+\frac{1}{2R^2}\frac{P_{1m'}}{a}\cos^2(\delta_p)\left(G_{10}^{(1)mm'}+\frac{1}{2}\cos^2(\delta_p)G_{11}^{(1)mm'}\right)\Bigg] \\
&+\pi{k_0}^4\cos^4(\delta_p)\left[\frac{3}{2R^2}\left(G_{03}^{(1)mm'}+G_{04}^{(1)mm'}\right)+\frac{1}{8R^4}\cos^8(\delta_p)\left(G_{07}^{(1)mm'}+G_{12}^{(1)mm'}\right)\right], \qquad (16a)
\end{aligned}
$$

$$
\begin{aligned}
{\beta_1}^{(1)mm'} &= -j\omega\mu_0\pi s\Bigg\{G_{13}^{(1)mm'}+\left(\frac{1}{2}\cos^2(\delta_p)+\frac{3}{4}\cos^4(\delta_p)\right)\frac{1}{R^2}G_{14}^{(1)mm'} \\
&+\left(\frac{1}{2}+\cos^2(\delta_p)\right)\frac{1}{R^2}G_{15}^{(1)mm'}-\frac{1}{2R^2}G_{00}^{(1)mm'}-\cos^2(\delta_p)\frac{1}{R^2}\frac{P^{'}_{1m'}}{a}G_{16}^{(1)mm'}\Bigg\}, \qquad (16b)
\end{aligned}
$$

where the elements of the matrices ($G_{00}^{(1)mm'}$, etc.) are given in [20]. Similarly, the rest of the elements on the left side in Eqs. (15a)-(15d) are obtained. We establish an algebraic system of four equations with four unknowns. All the elements of the matrices in the Laplace transform domain are dependent on the step's angle of the helix (δ_p), the Bessel functions; the dielectric profile g(r); the transverse derivative $g_r(r)$; and (r, θ).

The elements of the boundary conditions (e.g., $\widehat{(BC2)}_1$) at $\zeta = 0^+$ on the right side in (15b) are dependent on the step's angle δ_p as follows :

$$
\widehat{(BC2)}_1 = \int_0^{2\pi}\int_0^a (BC2)\sin\theta J_1(P_{1m}r/a)rdrd\theta,
$$

where

$$
(BC2) = \left[\left(s^2+k^2h_\zeta^2\right)\left(sE_{\zeta_0}+E^{'}_{\zeta_0}\right)\right]+j\omega\mu_0H_{\theta_0}sg_rh_\zeta^2
$$

$$+\frac{2}{R}h_\zeta \sin\theta\left(j\omega\mu_0 H_{\theta_0}s + k^2 E_{r_0}h_\zeta\right) + \frac{2}{R}h_\zeta\cos\theta\left(-j\omega\mu_0 H_{r_0}s + k^2 E_{\theta_0}h_\zeta\right) + k^2 h_\zeta^3 E_{r_0}g_r,$$

and for $h_\zeta = 1 + (r/R)\sin\theta\cos^2(\delta_p)$.

The boundary conditions at $\zeta = 0^+$ for TEM_{00} mode in excitation become to:

$$\widehat{(BC2)}_1 = 2\pi\left\{\int_0^a Q(r)(k(r)+js)J_{1m}(P_{1m}r/a)rdr\right\}\delta_{1n}$$
$$+\frac{4js\pi}{R^2}\cos^2(\delta_p)\left\{\int_0^a Q(r)k(r)J_{1m}(P_{1m}r/a)r^2dr\right\}\delta_{1n}$$

$$+\frac{9\pi}{2R^2}\cos^4(\delta_p)\left\{\int_0^a Q(r)k^2(r)J_{1m}(P_{1m}r/a)r^3dr\right\}\delta_{1n}$$
$$+\frac{3js\pi}{2R^2}\cos^4(\delta_p)\left\{\int_0^a Q(r)k(r)J_{1m}(P_{1m}r/a)r^3dr\right\}\delta_{1n}$$

$$+\frac{8\pi}{R^2}\cos^2(\delta_p)\left\{\int_0^a Q(r)k^2(r)J_{1m}(P_{1m}r/a)r^2dr\right\}\delta_{1n} \quad (17)$$

where :

$$Q(r) = \frac{E_0}{n_c(r)+1}g_r\exp\left(-(r/w_o)^2\right).$$

Similarly, the remaining elements of the boundary conditions at $\zeta = 0^+$ are obtained. The matrix system of Eqs.(15a)-(15d) is solved to obtain the coefficients (A_1, B_1, etc).

According to the Gaussian beams [23] the parameter w_0 is the minimum spot-size at the plane z=0, and the electric field at the plane z=0 is given by $E = E_0\exp[-(r/w_o)^2]$. The modes excited at ζ = 0 in the waveguide by the conventional CO_2 laser IR radiation (λ=10.6 μm) are closer to the TEM polarization of the laser radiation. The TEM_{00} mode is the fundamental and most important mode. This means that a cross-section of the beam has a Gaussian intensity distribution. The relation between the electric and magnetic fields [23] is given by $E/H = \sqrt{\mu_0/\epsilon_0} \equiv \eta_0$, where η_0 is the intrinsic wave impedance. Suppose that the electric field is parallel to the y-axis. Thus the components of E_y and H_x are written by the fields $E_y = E_0$ $\exp[-(r/w_o)^2]$ and $H_x = -(E_0/\eta_0)\exp[-(r/w_o)^2]$.

After a Gaussian beam passes through a lens and before it enters to the waveguide, the waist cross-sectional diameter ($2w_0$) can then be approximately calculated for a parallel incident beam by means of w_0=$\lambda/(\pi\ \theta) \simeq$ (f λ)/(π w). This approximation is justified if the parameter w_0 is much larger than the wavelength λ. The parameter of the waist cross-sectional diameter ($2w_0$) is taken into account in our method, instead of the focal length of the lens (f). The initial fields at $\zeta = 0^+$ are formulated by using the Fresnel coefficients of the transmitted fields [24] as follows

$$E_{r_0}^+(r) = T_E(r)(E_0 e^{-(r/w_o)^2}\sin\theta), \quad (18a)$$

$$E_{\theta_0}^{+} = T_E(r)(E_0 e^{-(r/w_o)^2}\cos\theta), \tag{18b}$$

$$H_{r_0}^{+} = -T_H(r)((E_0/\eta_0)e^{-(r/w_o)^2}\cos\theta), \tag{18c}$$

$$H_{\theta_0}^{+} = T_H(r)((E_0/\eta_0)e^{-(r/w_o)^2}\sin\theta), \tag{18d}$$

where $E_{\zeta_0}^{+} = H_{\zeta_0}^{+} = 0$, $T_E(r) = 2/[(n(r)+1]$, $T_H(r) = 2n(r)/[(n(r)+1]$, and $n(r) = [\epsilon_r(r)]^{1/2}$. The index of refraction is denoted by $n(r)$.

The transverse components of the fields are finally expressed in a form of *transfer matrix functions* for an arbitrary value of δ_p as follows:

$$\begin{aligned} E_r(r,\theta,\zeta) = E_{r0}^{+}(r)e^{-jkh_\zeta\zeta} - \frac{j\omega\mu_0}{R}h_\zeta\cos^2\theta\cos^2(\delta_p)\sum_{m'}C_{S1}^{m'}(\zeta)J_1(\psi) \\ -\frac{j\omega\mu_0}{R}h_\zeta\sin\theta\cos\theta\cos^2(\delta_p)\sum_{m'}D_{S1}^{m'}(\zeta)J_1(\psi) + \frac{j\omega\mu_0}{r}h_\zeta^2\sin\theta\sum_{m'}C_{S1}^{m'}(\zeta)J_1(\psi) \\ -\frac{j\omega\mu_0}{r}h_\zeta^2\cos\theta\sum_{m'}D_{S1}^{m'}(\zeta)J_1(\psi) + \frac{1}{R}\sin\theta\cos\theta\cos^2(\delta_p)\sum_{m'}A_{S2}^{m'}(\zeta)J_1(\xi) \\ +\frac{1}{R}\sin^2\theta\cos^2(\delta_p)\sum_{m'}B_{S2}^{m'}(\zeta)J_1(\xi) + h_\zeta\cos\theta\sum_{m'}A_{S2}^{m'}(\zeta)\frac{dJ_1}{dr}(\xi) \\ +h_\zeta\sin\theta\sum_{m'}B_{S2}^{m'}(\zeta)\frac{dJ_1}{dr}(\xi), \end{aligned} \tag{19}$$

where $h_\zeta = 1 + (r/R)\sin\theta\cos^2(\delta_p)$, R is the radius of the cylinder, δ_p is the the step's angle, $\psi = [P'_{1m'}(r/a)]$ and $\xi = [P_{1m'}(r/a)]$. The coefficients are given in the above equation, for instance

$$A_{S1}^{m'}(\zeta) = \mathcal{L}^{-1}\left\{\frac{A_{1m'}(s)}{s^2 + k^2(r)h_\zeta^2}\right\}, \tag{20a}$$

$$A_{S2}^{m'}(\zeta) = \mathcal{L}^{-1}\left\{\frac{sA_{1m'}(s)}{s^2 + k^2(r)h_\zeta^2}\right\}, \tag{20b}$$

where

$$m' = 1,...N, \qquad 3 \le N \le 50. \tag{20c}$$

Similarly, the other transverse components of the output fields are obtained. The first fifty roots (zeros) of the equations $J_1(x) = 0$ and $dJ_1(x)/dx = 0$ may be found in tables [25-26].

The inverse Laplace transform is performed in this study by a direct numerical integration in the Laplace transform domain by the residue method, as follows

$$f(\zeta) = \mathcal{L}^{-1}[\tilde{f}(s)] = \frac{1}{2\pi j}\int_{\sigma-j_\infty}^{\sigma+j_\infty}\tilde{f}(s)e^{s\zeta}ds = \sum_n Res[e^{s\zeta}\tilde{f}(s); S_n]. \tag{21}$$

By using the inverse Laplace transform (21) we can compute the output transverse components in the real plane and the output power density at each point at ζ=(R ϕ_c)$/cos(\delta_p)$.

The integration path in the right side of the Laplace transform domain includes all the singularities according to Eq.(21). All the points S_n are the poles of $\tilde{f}(s)$ and $Res[e^{s\zeta}\tilde{f}(s); S_n]$ represent the residue of the function in a specific pole. According to the residue method, two dominant poles for the helical waveguide are given by

$$s = \pm j\, k(r) h_\zeta = \pm j\, k(r)\left(1 + \frac{r}{R}\sin\theta\cos^2(\delta_p)\right).$$

Finally, knowing all the transverse components, the ζ component of the average-power density Poynting vector is given by

$$S_{av} = \frac{1}{2} Re\left\{ E_r {H_\theta}^* - E_\theta {H_r}^* \right\} \quad , \tag{22}$$

where the asterisk indicates the complex conjugate.

The total average-power transmitted along the guide in the ζ direction can now be obtained by the integral of Eq.(22) over the waveguide cross section. Thus, the output power transmission is given by

$$T = \frac{1}{2}\int_0^{2\pi}\int_0^a Re\left\{ E_r {H_\theta}^* - E_\theta {H_r}^* \right\} r dr d\theta \quad . \tag{23}$$

3.2 Solution of the wave equations for the helical coordinate system (x, y, ζ).

The method is based on Fourier coefficients of the transverse dielectric profile and those of the input wave profile. Laplace transform is necessary to obtain the comfortable and simple input-output connections of the fields. This model is useful for the analysis of dielectric waveguides in the microwave and the millimeter-wave regimes, for diffused optical waveguides in integrated optics. The output power transmission and the output power density are improved by increasing the step's angle or the radius of the cylinder of the helical waveguide, especially in the cases of space curved waveguides.

We assume that for most materials, the permeability μ is equal to that of free space ($\mu = \mu_0$). The wave equations for the electric and magnetic field components in the inhomogeneous dielectric medium $\epsilon(x, y)$ are given by the wave equations (5a) and (5b), respectively. The transverse dielectric profile $(\epsilon(x, y))$ is defined as $\epsilon_0(1 + \chi_0 g(x, y))$, where ϵ_0 represents the vacuum dielectric constant, $g(x, y)$ is its profile function in the waveguide, and χ_0 is the susceptibility of the dielectric material. The normalized transverse derivatives of the dielectric profile $g(x, y)$ are defined as $(1/\epsilon(x, y))[(\partial/\partial x)\epsilon(x, y)]$ and $(1/\epsilon(x, y))[(\partial/\partial y)\epsilon(x, y)]$, respectively. From the helical transformation of Eqs. 1 we can derive the Laplacian of the vector $\boldsymbol{E}$ (i.e., $\nabla^2\boldsymbol{E}$), and obtain the wave equations for the electric and magnetic fields in the inhomogeneous dielectric medium. It is necessary to find the values of $\nabla \cdot \boldsymbol{E}$, $\nabla(\nabla \cdot \boldsymbol{E})$, $\nabla \times \boldsymbol{E}$, and $\nabla \times (\nabla \times \boldsymbol{E})$ in order to obtain the value of $\nabla^2\boldsymbol{E}$, where $\nabla^2\boldsymbol{E} = \nabla(\nabla \cdot \boldsymbol{E}) - \nabla \times (\nabla \times \boldsymbol{E})$. All these values are dependent on the metric coefficients (4a,b,c).

The components of $\nabla^2\boldsymbol{E}$ are given by

$$(\nabla^2\boldsymbol{E})_x = \nabla^2 E_x - \frac{1}{R^2 h_\zeta^2}\cos^2(\delta_p)E_x - 2\frac{1}{Rh_\zeta^2}\cos^2(\delta_p)\frac{\partial}{\partial\zeta}E_\zeta, \tag{24a}$$

$$(\nabla^2\boldsymbol{E})_y = \nabla^2 E_y, \tag{24b}$$

$$(\nabla^2\boldsymbol{E})_\zeta = \nabla^2 E_\zeta - \frac{1}{R^2 h_\zeta^2}\cos^2(\delta_p)E_\zeta + 2\frac{1}{Rh_\zeta^2}\cos^2(\delta_p)\frac{\partial}{\partial\zeta}E_x, \tag{24c}$$

where

$$\nabla^2 = \frac{\partial^2}{\partial x^2} + \frac{\partial^2}{\partial y^2} + \frac{1}{h_\zeta^2}\frac{\partial^2}{\partial\zeta^2} + \frac{1}{Rh_\zeta}\cos^2(\delta_p)\frac{\partial}{\partial x}, \tag{24d}$$

and for $h_\zeta = 1 + (x/R)\cos^2(\delta_p)$.

The wave equations (5a) and (5b) are written in the form

$$(\nabla^2\boldsymbol{E})_i + k^2 E_i + \partial_i(E_x g_x + E_y g_y) = 0, \tag{25a}$$

$$(\nabla^2\boldsymbol{H})_i + k^2 H_i + \partial_i(H_x g_x + H_y g_y) = 0, \tag{25b}$$

where i=x, y, ζ. The *local* wavenumber parameter is given by $k = \omega\sqrt{\mu\epsilon(x,y)} = k_0\sqrt{1+\chi_0 g(x,y)}$, and the free-space wavenumber is given by $k_0 = \omega\sqrt{\mu_0\epsilon_0}$. The expression $(\nabla^2\boldsymbol{E})_x$, for instance, is given according to Eq. (24a).

The transverse Laplacian operator is defined according to Eq. (12), where

$$h_\zeta^2 = 1 + \frac{2x}{R}\cos^2(\delta_p) + \left(\frac{x}{R}\right)^2\cos^4(\delta_p).$$

The metric coefficient h_ζ is a function of x, thus we defined

$$h_\zeta = 1 + p_\zeta(x) \ , \ p_\zeta(x) = \cos^2(\delta_p)(x/R), \tag{26a}$$

$$h_\zeta^2 = 1 + q_\zeta(x) \ , \ q_\zeta(x) = \cos^2(\delta_p)(2/R)x. \tag{26b}$$

The Laplace transform (Eq. (13)) is applied on the ζ-dimension, where $a(\zeta)$ represents any ζ-dependent variables and $\zeta = (R\phi_c)/\cos(\delta_p)$. Laplace transform on the differential wave equations is needed to obtain the wave equations (and thus also the output fields) that are expressed directly as functions of the transmitted fields at the entrance of the waveguide at $\zeta = 0^+$. Thus, the Laplace transform is necessary to obtain the comfortable and simple *input-output* connections of the fields.

By substitution of Eqs. (24a)-(24c) into Eqs. (25a), by using the Laplace transform (13), and multiply by h_ζ^2, Eqs. (5a) are described in the Laplace transform domain in the form

$$h_\zeta^2\left(\nabla_\perp^2 + \frac{s^2}{h_\zeta^2} + k^2\right)\tilde{E}_x + h_\zeta^2\partial_x\left(\tilde{E}_x g_x + \tilde{E}_y g_y\right) + h_\zeta\frac{1}{R}\cos^2(\delta_p)\partial_x\left(\tilde{E}_x\right)$$

$$-\frac{2}{R}\cos^2(\delta_p)s\tilde{E}_\zeta = \left(sE_{x_0} + E'_{x_0}\right) - \frac{2}{R}\cos^2(\delta_p)E_{\zeta_0}, \tag{27a}$$

$$h_\zeta^2\left(\nabla_\perp^2 + \frac{s^2}{h_\zeta^2} + k^2\right)\tilde{E}_y + h_\zeta^2\partial_y\left(\tilde{E}_x g_x + \tilde{E}_y g_y\right) + h_\zeta\frac{1}{R}\cos^2(\delta_p)\partial_x\left(\tilde{E}_y\right) = \left(sE_{y_0} + E'_{y_0}\right), \tag{27b}$$

$$h_\zeta^2\left(\nabla_\perp^2 + \frac{s^2}{h_\zeta^2} + k^2\right)\tilde{E}_\zeta + sh_\zeta^2\left(\tilde{E}_x g_x + \tilde{E}_y g_y\right) + h_\zeta\frac{1}{R}\cos^2(\delta_p)\partial_x\left(\tilde{E}_\zeta\right) + \frac{2}{R}\cos^2(\delta_p)s\tilde{E}_x = \left(sE_{\zeta_0} + E'_{\zeta_0}\right) + \frac{2}{R}\cos^2(\delta_p)E_{x_0} + h_\zeta^2\left(E_{x_0}g_x + E_{y_0}g_y\right), \tag{27c}$$

where the transverse Laplacian operator is defined according to (12), E_{x_0}, E_{y_0}, $E_{\zeta 0}$ are the initial values of the corresponding fields at $\zeta = 0$, i.e. $E_{x_0} = E_x(x, y, \zeta = 0)$ and $E'_{x_0} = \frac{\partial}{\partial\zeta}E_x(x, y, \zeta)|_{\zeta=0}$.

A Fourier transform is applied on the transverse dimension

$$\bar{g}(k_x, k_y) = \mathcal{F}\{g(x, y)\} = \int_x\int_y g(x, y)e^{-jk_x x - jk_y y}dxdy, \tag{28}$$

and the differential equation (27(a)) is transformed to an algebraic form in the (ω, s, k_x, k_y) space, as follows

$$\begin{aligned} &k_\zeta^2\bar{\tilde{E}}_x + s^2\bar{\tilde{E}}_x + k_o^2\chi_o\bar{g} * \bar{\tilde{E}}_x + jk_x\left(\bar{g}_x * \bar{\tilde{E}}_x + \bar{g}_y * \bar{\tilde{E}}_y\right) - \tfrac{2}{R}\cos^2(\delta_p)s\bar{\tilde{E}}_\zeta + \bar{q}_\zeta * \left(k_\zeta^2\right)\bar{\tilde{E}}_x + \\ &k_o^2\chi_o\bar{q}_\zeta * \left(\bar{g} * \bar{\tilde{E}}_x\right) + j\bar{q}_\zeta * \left[k_x\left(\bar{g}_x * \bar{\tilde{E}}_x + \bar{g}_y * \bar{\tilde{E}}_y\right)\right] \\ &+\tfrac{1}{R}\cos^2(\delta_p)\left(jk_x\right)\bar{\tilde{E}}_x + \tfrac{1}{R}\cos^2(\delta_p)j\bar{p}_\zeta * \left(k_x\bar{\tilde{E}}_x\right) \\ &= \left(s\bar{E}_{x_0} + \bar{E}'_{x_0}\right) - \tfrac{1}{sR}\cos^2(\delta_p)\left(s\bar{E}_{\zeta_0} + \bar{E}'_{\zeta_0}\right), \end{aligned} \tag{29}$$

where $k_\zeta = \sqrt{k_o^2 - k_x^2 - k_y^2}$. Similarly, the other differential equations are obtained. The asterisk symbol denotes the convolution operation $\bar{g} * \bar{E} = \mathcal{F}\{g(x, y)E(x, y)\}$. The method of images is applied to satisfy the conditions $\hat{n} \times E = 0$ and $\hat{n} \cdot (\bigtriangledown \times E) = 0$ on the surface of the ideal metallic waveguide walls, where $\hat{n}$ is a unit vector perpendicular to the surface. The metric coefficient h_ζ is a function of x (Eqs. (26a) and (26b)). Thus the elements of the matrices $\mathbf{P^{(0)}}$ and $\mathbf{Q^{(0)}}$ are defined as:

$$\bar{p_\zeta}^{(o)}_{(n,m)} = \frac{1}{4ab}\int_{-a}^{a}\int_{-b}^{b} p_\zeta(x)\ e^{-j(n\frac{\pi}{a}x + m\frac{\pi}{b}y)}\ dxdy, \tag{30a}$$

$$\bar{q_\zeta}^{(o)}_{(n,m)} = \frac{1}{4ab}\int_{-a}^{a}\int_{-b}^{b} q_\zeta(x)\ e^{-j(n\frac{\pi}{a}x + m\frac{\pi}{b}y)}\ dxdy, \tag{30b}$$

and the matrices $\mathbf{P^{(1)}}$ and $\mathbf{Q^{(1)}}$ are defined as:

$$\mathbf{P^{(1)}} = \left(\mathbf{I} + \mathbf{P^{(0)}}\right), \quad \mathbf{Q^{(1)}} = \left(\mathbf{I} + \mathbf{Q^{(0)}}\right), \tag{30c,d}$$

where $\mathbf{I}$ is the unity matrix.

Equation (29) and similarly, the two other equations are rewritten in a matrix form as follows

$$\mathbf{K^{(0)}}E_x + \frac{k_o^2\chi_0}{2s}\mathbf{Q^{(1)}}\mathbf{G}E_x + \frac{jk_{ox}}{2s}\mathbf{Q^{(1)}}\mathbf{N}\left(\mathbf{G_x}E_x + \mathbf{G_y}E_y\right)$$

$$-\frac{1}{R}\cos^2(\delta_p)E_\zeta + \mathbf{Q^{(0)}}\mathbf{K1^{(0)}}E_x + \frac{1}{2sR}\cos^2(\delta_p)jk_{ox}\mathbf{P^{(1)}}\mathbf{N}E_x = \hat{E}_{x_0} - \frac{1}{sR}\cos^2(\delta_p)\bar{E}_{\zeta_0}, \tag{31a}$$

$$\mathbf{K^{(0)}}E_y + \frac{k_o^2\chi_0}{2s}\mathbf{Q^{(1)}}\mathbf{G}E_y + \frac{jk_{oy}}{2s}\mathbf{Q^{(1)}}\mathbf{M}\left(\mathbf{G_x}E_x + \mathbf{G_y}E_y\right)$$

$$+\mathbf{Q^{(0)}}\mathbf{K1^{(0)}}E_y + \frac{1}{2sR}\cos^2(\delta_p)jk_{ox}\mathbf{P^{(1)}}\mathbf{N}E_y = \hat{E}_{y_0}, \tag{31b}$$

$$\mathbf{K^{(0)}}E_\zeta + \frac{k_o^2\chi_0}{2s}\mathbf{Q^{(1)}}\mathbf{G}E_\zeta + \frac{1}{2}\mathbf{Q^{(1)}}\left(\mathbf{G_x}E_x + \mathbf{G_y}E_y\right) + \frac{1}{R}\cos^2(\delta_p)E_x$$

$$+\mathbf{Q^{(0)}}\mathbf{K1^{(0)}}E_\zeta + \frac{1}{2sR}\cos^2(\delta_p)jk_{ox}\mathbf{P^{(1)}}\mathbf{N}E_\zeta = \hat{E}_{\zeta_0} + \frac{1}{sR}\cos^2(\delta_p)E_{x_0} + \frac{1}{2s}\mathbf{Q^{(1)}}\left(\mathbf{G_x}E_{x_0} + \mathbf{G_y}E_{y_0}\right), \tag{31c}$$

where the initial-value vectors, $\hat{E}_{x_0}$, $\hat{E}_{y_0}$, and $\hat{E}_{\zeta_0}$ are defined from the terms $(s\bar{E}_{x_0} + \bar{E}'_{x_0})/2s$, $(s\bar{E}_{y_0} + \bar{E}'_{y_0})/2s$, and $(s\bar{E}_{\zeta_0} + \bar{E}'_{\zeta_0})/2s$, respectively.

The elements of the diagonal matrices $\mathbf{K^{(0)}}$, $\mathbf{M}$, $\mathbf{N}$ and $\mathbf{K^{(1)}}$ are defined as

$$K^{(0)}{}_{(n,m)(n',m')} = \left\{\left[k_o^2 - (n\pi/a)^2 - (m\pi/b)^2 + s^2\right]/2s\right\}\delta_{nn'}\delta_{mm'}, \tag{32a}$$

$$M_{(n,m)(n',m')} = m\delta_{nn'}\delta_{mm'}, \tag{32b}$$

$$N_{(n,m)(n',m')} = n\delta_{nn'}\delta_{mm'}, \tag{32c}$$

$$K^{(1)}{}_{(n,m)(n',m')} = \left\{\left[k_o^2 - (n\pi/a)^2 - (m\pi/b)^2\right]/2s\right\}\delta_{nn'}\delta_{mm'}, \tag{32d}$$

where $\delta_{nn'}$ and $\delta_{mm'}$ are the Kronecker delta functions.

The modified wave-number matrices are defined as

$$\mathbf{D_x} \equiv \mathbf{K^{(0)}} + \mathbf{Q^{(0)}}\mathbf{K1^{(0)}} + \frac{k_o^2\chi_0}{2s}\mathbf{Q^{(1)}}\mathbf{G} + \frac{jk_{ox}}{2s}\mathbf{Q^{(1)}}\mathbf{N}\mathbf{G_x} + \frac{1}{2sR}\cos^2(\delta_p)jk_{ox}\mathbf{P^{(1)}}\mathbf{N}, \tag{33a}$$

$$\mathbf{D_y} \equiv \mathbf{K^{(0)}} + \mathbf{Q^{(0)}}\mathbf{K1^{(0)}} + \frac{k_o^2\chi_0}{2s}\mathbf{Q^{(1)}}\mathbf{G} + \frac{1}{2sR}\cos^2(\delta_p)jk_{ox}\mathbf{P^{(1)}}\mathbf{N} + \frac{jk_{oy}}{2s}\mathbf{Q^{(1)}}\mathbf{M}\mathbf{G_y}, \tag{33b}$$

$$\mathbf{D_\zeta} \equiv \mathbf{K^{(0)}} + \mathbf{Q^{(0)}K1^{(0)}} + \frac{k_o^2\chi_0}{2s}\mathbf{Q^{(1)}G} + \frac{1}{2sR}\cos^2(\delta_p)jk_{ox}\mathbf{P^{(1)}N}. \tag{33c}$$

Thus, Eqs. (31a)-(31c) result in

$$\mathbf{D_x}E_x = \hat{E}_{x_0} - \frac{jk_{ox}}{2s}\mathbf{Q^{(1)}NG_y}E_y - \frac{1}{sR}\cos^2(\delta_p)E_{\zeta_0} + \frac{1}{R}\cos^2(\delta_p)E_\zeta, \tag{34a}$$

$$\mathbf{D_y}E_y = \hat{E}_{y_0} - \frac{jk_{oy}}{2s}\mathbf{Q^{(1)}MG_x}E_x, \tag{34b}$$

$$\mathbf{D_\zeta}E_\zeta = \hat{E}_{\zeta_0} + \frac{1}{2s}\mathbf{Q^{(1)}}\left(\mathbf{G_x}E_{x_0} + \mathbf{G_y}E_{y_0}\right) - \frac{1}{2}\mathbf{Q^{(1)}}\left(\mathbf{G_x}E_x + \mathbf{G_y}E_y\right) + \frac{1}{sR}\cos^2(\delta_p)E_{x_0} - \frac{1}{R}\cos^2(\delta_p)E_x. \tag{34c}$$

After some algebraic steps, the components of the electric field are formulated as follows:

$$E_x = \left\{\mathbf{D_x} + \alpha_1\mathbf{Q^{(1)}M_1Q^{(1)}M_2} + \frac{1}{R}\cos^2(\delta_p)\mathbf{D_\zeta}^{-1}\right.$$

$$\left.\cdot\left(-\frac{1}{2}\mathbf{Q^{(1)}G_x} + \frac{1}{2}\alpha_2\mathbf{Q^{(1)}M_3Q^{(1)}M_2} - \frac{1}{R}\cos^2(\delta_p)\mathbf{I}\right)\right\}^{-1}$$

$$\left(\hat{E}_{x_0} - \frac{1}{sR}\cos^2(\delta_p)E_{\zeta_0} - \alpha_3\mathbf{Q^{(1)}M_1}\hat{E}_{y_0} + \frac{1}{R}\cos^2(\delta_p)\mathbf{D_\zeta}^{-1}\left(\hat{E}_{\zeta_0} + \frac{1}{sR}\cos^2(\delta_p)E_{x_0} + \right.\right.$$

$$\left.\left.\frac{1}{2s}\mathbf{Q^{(1)}}(\mathbf{G_x}E_{x_0} + \mathbf{G_y}E_{y_0}) - \frac{1}{2}\mathbf{Q^{(1)}M_3}\hat{E}_{y_0}\right)\right), \tag{35a}$$

$$E_y = \mathbf{D_y}^{-1}\left(\hat{E}_{y_0} - \frac{jk_{oy}}{2s}\mathbf{Q^{(1)}MG_x}E_x\right), \tag{35b}$$

$$E_\zeta = \mathbf{D_\zeta}^{-1}\left\{\hat{E}_{\zeta_0} + \frac{1}{2s}\mathbf{Q^{(1)}}\left(\mathbf{G_x}E_{x_0} + \mathbf{G_y}E_{y_0}\right) - \frac{1}{2}\mathbf{Q^{(1)}}\left(\mathbf{G_x}E_x + \mathbf{G_y}E_y\right)\right.$$

$$\left. - \frac{1}{R}\cos^2(\delta_p)E_x + \frac{1}{sR}\cos^2(\delta_p)E_{x_0}\right\}, \tag{35c}$$

where:

$$\alpha_1 = \frac{k_{ox}k_{oy}}{4s^2}, \quad \alpha_2 = \frac{jk_{oy}}{2s}, \quad \alpha_3 = \frac{jk_{ox}}{2s}, \quad \mathbf{M_1} = \mathbf{NG_y}\mathbf{D_y}^{-1}, \quad \mathbf{M_2} = \mathbf{MG_x}, \quad \mathbf{M_3} = \mathbf{G_y}\mathbf{D_y}^{-1}.$$

These equations describe the transfer relations between the spatial spectrum components of the output and input waves in the dielectric waveguide. Similarly, the other components of the magnetic field are obtained. The transverse field profiles are computed by the inverse

Laplace and Fourier transforms, as follows

$$E_y(x,y,\zeta) = \sum_n \sum_m \int_{\sigma-j_\infty}^{\sigma+j_\infty} E_y(n,m,s) e^{jnk_{ox}x + jmk_{oy}y + s\zeta} ds. \tag{36}$$

The inverse Laplace transform is performed in this study by a direct numerical integration on the s-plane by the method of Gaussian Quadrature. The integration path in the right side of the s-plane includes all the singularities, as proposed by Salzer [27-28]

$$\int_{\sigma-j_\infty}^{\sigma+j_\infty} e^{s\zeta} E_y(s) ds = \frac{1}{\zeta} \int_{\sigma-j_\infty}^{\sigma+j_\infty} e^{p} E_y(p/\zeta) dp = \frac{1}{\zeta} \sum_{i=1}^{15} w_i E_y(s = p_i/\zeta), \tag{37}$$

where w_i and p_i are the weights and zeros, respectively, of the orthogonal polynomials of order 15. The Laplace variable s is normalized by p_i/ζ in the integration points, where $\mathrm{Re}(p_i) > 0$ and all the poles should be localized in their left side on the Laplace transform domain. This approach of a direct integral transform does not require as in other methods, to deal with each singularity separately.

The ζ component of the average-power density of the complex Poynting vector is given by

$$S_{av} = \frac{1}{2} Re\left\{ E_x {H_y}^* - E_y {H_x}^* \right\}, \tag{38}$$

where the asterisk indicates the complex conjugate. The active power is equal to the real part of the complex Poynting vector. The total average-power transmitted along the guide in the ζ direction is given by a double integral of Eq. (38). A Fortran code is developed using NAG subroutines [29]. Several examples computed on a Unix system are presented in the next section.

4. Numerical results

An example of the circular cross section of the helical waveguide is shown in Fig. 3(a). An example of the rectangular dielectric slab of the helical waveguide is shown in Fig. 3(b), and an example of the rectangular cross section with a circular dielectric profile of the helical waveguide is shown in Fig. 3(c). The results of the output transverse components of the fields and the output power density ($|S_{av}|$) (e.g., Fig. 4(a)) show the behavior of the solutions for the TEM_{00} mode in excitation, for the straight waveguide ($R \to \infty$). The result of the output power density (Fig. 4(a)) is compared also to the result of published experimental data [30] as shown also in Fig. 4(b). This comparison shows good agreement (a Gaussian shape) as expected, except for the secondary small propagation mode. The experimental result (Fig. 4(b)) is affected by the additional parameters (e.g., the roughness of the internal wall of the waveguide) which are not taken theoretically into account. In this example with the circular cross section (Fig. 3(a)), the length of the straight waveguide is 1 m, the diameter (2a) of the waveguide is 2 mm, the thickness of the dielectric layer [$d_{(AgI)}$] is 0.75 μm, and the minimum spot-size (w_0) is 0.3 mm. The refractive indices of the air, the dielectric layer (AgI) and the metallic layer (Ag) are $n_{(0)} = 1$, $n_{(AgI)} = 2.2$, and $n_{(Ag)} = 13.5 - j75.3$, respectively.

The value of the refractive index of the material at a wavelength of λ=10.6 μm is taken from the table compiled by Miyagi, et al. [6]. The toroidal dielectric waveguide is demonstrated in Fig. 4(c). The experimental result is demonstrated in Fig. 4(d). This experimental result was obtained from the measurements of the transmitted CO_2 laser radiation (λ=10.6 μm) propagation through a hollow tube covered on the bore wall with silver and silver-iodide layers (Fig. 3(a)), where the initial diameter (ID) is 1 mm (namely, small bore size).

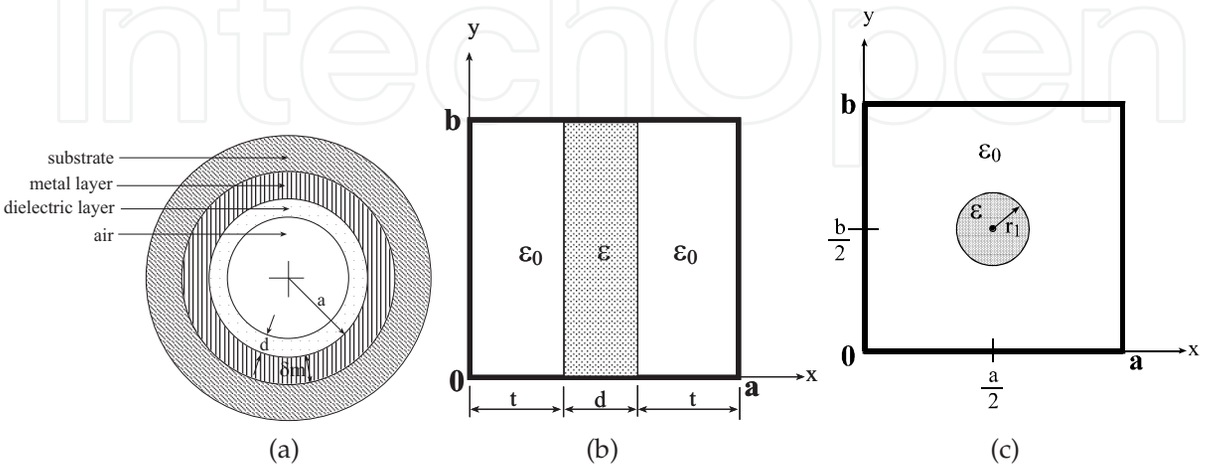

Figure 3. (a) An example of the circular cross section of the helical waveguide. (b) An example of the rectangular dielectric slab of the helical waveguide. (c) An example of the rectangular cross section with a circular dielectric profile of the helical waveguide.

The output modal profile is greatly affected by the bending, and the theoretical and experimental results (Figs. 4(c)-4(d)) show that in addition to the main propagation mode, several other secondary modes and asymmetric output shape appear. The amplitude of the output power density ($|S_{av}|$) is small as the bending radius (R) is small, and the shape is far from a Gaussian shape. This result agrees with the experimental results, but not for all the propagation modes. The experimental result (Fig. 4(d)) is affected by the bending and additional parameters (e.g., the roughness of the internal wall of the waveguide) which are not taken theoretically into account. In this example, a=0.5 mm, R=0.7 m, $\phi=\pi/2$, and ζ= 1 m. The thickness of the dielectric layer [$d_{(AgI)}$] is 0.75 μm (Fig. 3(a)), and the minimum spot size (w_0) is 0.2 mm. The values of the refractive indices of the air, the dielectric layer (AgI) and the metallic layer (Ag) are $n_{(0)} = 1$, $n_{(AgI)} = 2.2$, and $n_{(Ag)} = 13.5 - j75.3$, respectively. In both theoretical and experimental results (Figs. 4(c)-4(d)) the shapes of the output power density for the curved waveguide are not symmetric. The output modal profile is greatly affected by the bending, and the theoretical and experimental results (Figs. 4(c)-4(d)) show that in addition to the main propagation mode, several other secondary modes and asymmetric output shape appear. The amplitude of the output power density ($|S_{av}|$) is small as the bending radius (R) is small, and the shape is far from a Gaussian shape. This result agrees with the experimental results, but not for all the propagation modes. The experimental result (Fig. 4(d)) is affected by the bending and additional parameters (e.g., the roughness of the internal wall of the waveguide) which are not taken theoretically into account. In this example, a=0.5 mm, R=0.7 m, $\phi=\pi/2$, and ζ= 1 m. The thickness of the dielectric layer [$d_{(AgI)}$] is 0.75 μm (Fig. 3(a)), and the minimum spot size (w_0) is 0.2 mm. The values of the

refractive indices of the air, the dielectric layer (AgI) and the metallic layer (Ag) are $n_{(0)} = 1$, $n_{(AgI)} = 2.2$, and $n_{(Ag)} = 13.5 - j75.3$, respectively. In both theoretical and experimental results (Figs. 4(c)-4(d)) the shapes of the output power density for the curved waveguide are not symmetric.

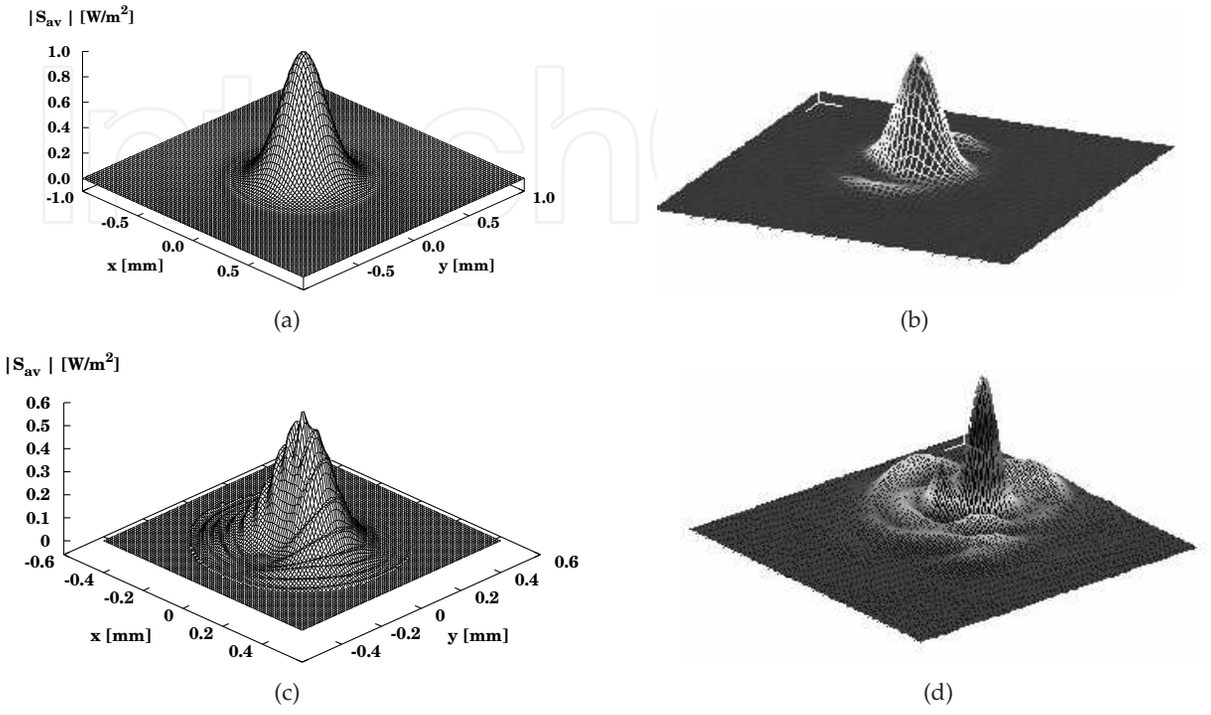

Figure 4. The output power density for R $\rightarrow \infty$, where a=1 mm, w_0 = 0.3 mm, and the length of the straight waveguide is 1 m. (a) theoretical result; (b) experimental result. The output power density for the toroidal dielectric waveguide, where a=0.5 mm, w_0 = 0.2 mm, R = 0.7 m, $\phi = \pi/2$, and ζ =1 m; (c) theoretical result; (d) experimental result. The other parameters are: $d_{(AgI)}$= 0.75 μm, λ = 10.6 μm, $n_{(0)}$ = 1, $n_{(AgI)}$ = 2.2, and $n_{(Ag)}$ = 13.5 - j 75.

Figures 5(a)-(b) show the results of the output power density as functions of the step's angle (e.g., δ_p =0.4, 0.8) and the radius of the cylinder (e.g., R=0.7 m). For these results ζ= 1 m, where a=1 mm, w_0 = 0.3 mm, n_d =2.2, and $n_{(Ag)}$ = 13.5 - j 75.3 (Fig. 3(a)). Fig. 5(a) shows that in addition to the main propagation mode, several other secondary modes appear, where δ_p = 0.4 and R=0.7 m. By increasing only the step's angle from δ_p = 0.4 to δ_p = 0.8 where R = 0.7 m, the amplitude of the output power density is greater (e.g., ($|S_{av}|$ = 0.7 W/m^2) and also the output shape is changed (Fig. 5(b)).

Let us compare the second theoretical model (e.g., Eq. 35(b)) with the known analytical theory [22] for the rectangular dielectric slab (Fig. 3(b)). For the given dimensions a and d, we find the values Λ and Ω according to the next transcendental equation for a dielectric slab (Fig. 3(b)).

According to our theoretical model we can calculate $E_{y_0}(n,m)$ and $g(n,m)$ as follows:

$$E_{y_0}(n,m) = \frac{1}{4ab}\int_{-a}^{a}\int_{-b}^{b} E_y(x,y,z=0)e^{-j(n\frac{\pi}{a}x+m\frac{\pi}{b}y)}dxdy,$$

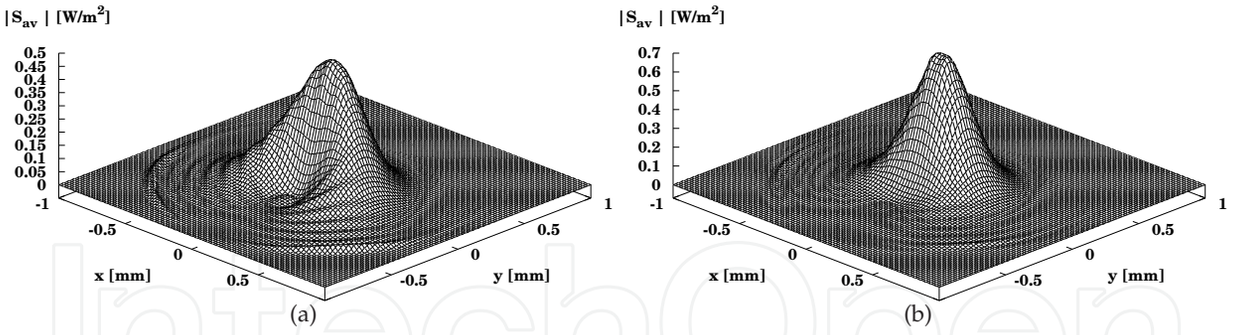

Figure 5. The results of the output power density as functions of the step's angle (δ_p) and the radius of the cylinder (R), where ζ= 1 m, a=1 mm, w_0 = 0.3 mm, n_d =2.2, and $n_{(Ag)}$ = 13.5 - j 75.3: (a). δ_p = 0.4, and R = 0.7 m; (b). δ_p = 0.8, and R = 0.7 m.

and

$$g(n,m) = \frac{1}{4ab}\int_{-a}^{a}\int_{-b}^{b} g(x,y)e^{-j(n\frac{\pi}{a}x+m\frac{\pi}{b}y)}dxdy.$$

The known solution for the dielectric slab modes based on transcendental equation [22] is given as follows

$$\begin{cases} E_{y1} = j\frac{k_z}{\epsilon_0}\sin(\nu x) & 0 < x < t \\ E_{y2} = j\frac{k_z}{\epsilon_0}\frac{\sin(\nu t)}{\cos(\mu(t-a/2))}\cos\left[\mu(x-a/2)\right] & t < x < t+d \\ E_{y3} = j\frac{k_z}{\epsilon_0}\sin\left[\nu(a-x)\right] & t+d < x < a \end{cases}, \tag{39}$$

where $\nu \equiv \sqrt{k_o^2 - k_z^2}$ and $\mu \equiv \sqrt{\epsilon_r k_o^2 - k_z^2}$ result from the transcendental equation

$$\left(\frac{a}{d}-1\right)\frac{d\mu}{2}\tan\left(\frac{d\mu}{2}\right) - (t\nu)\cot(t\nu) = 0.$$

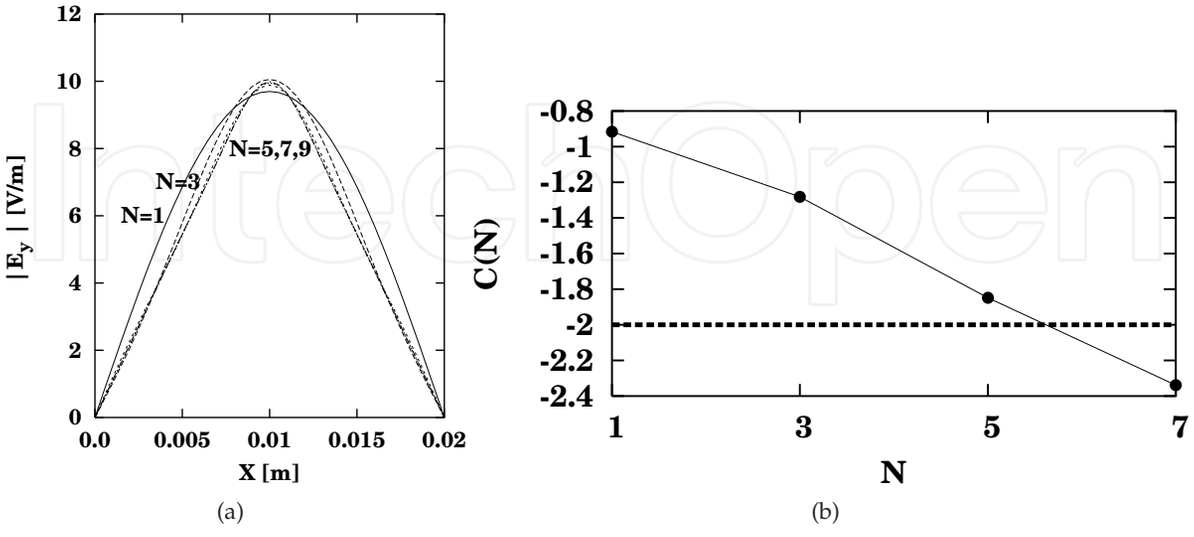

Figure 6. (a). A comparison between amplitude results of the theoretical model and the transcendental equation (a=2b=2 cm, d=3.3 mm, ϵ_r= 9, and λ= 6.9 cm; (b). The convergence of our theoretical results.

Eqs. (39) were substituted as the initial fields into the Eq. (35(b)) at $z = 0^+$ in the practical case of the straight waveguide (by letting R $\rightarrow \infty$ or by taking $\delta_p = \pi/2$) with the symmetrical slab profile (Fig. 3(b)). The result of the comparison between the theoretical model with the known solution [22] is shown in Fig. 6(a), where ϵ_r = 9, d=3.3 mm, and $\lambda = 6.9$ cm. The convergence of the numerical results as a function of the matrix order is shown in Fig. 6(b). The comparison is demonstrated for every order (N=1, 3, 5, 7, and 9). The order N determines the accuracy of the solution, and the convergence of the solution is verified by the criterion

$$C(N) \equiv log\left\{ \frac{max(|S_{av}^{N+2} - S_{av}^{N}|)}{|max(S_{av}^{N+2}) - min(S_{av}^{N})|} \right\}, \qquad N \geq 1, \tag{40}$$

for the E_y component of the fields (instead of S_{av}), where the number of the modes is equal to $(2N+1)^2$. The method of this model is based on Fourier coefficients, thus the accuracy of the method is dependent on the number of the modes in the system. Further we assume N = M. If the value of the criterion is less then -2, then the numerical solution is well converged. When N increases, then $E_y(N)$ approaches E_y. The value of the criterion between N=7 and N=9 is equal to -2.38 $\simeq$ -2, namely a hundredth part. The comparison between the theoretical mode-model and the known model [22] has shown good agreement. Note that we have two ways to compare between the results of our mode model with the other methods. The first way is to compare between the results of the output fields for every order (N=1, 3, 5, 7, and 9) with the final solution of the known method. The second way is to compare between the results of the output fields (according to our model) for every two orders (N=1,3, N=3,5, N=5,7, and N=7,9), until our numerical solution is well converged. This way is efficient in the cases that we have complicated problems that we cannot compare with the final solution of the known method.

The geometrical shape of a circular dielectric profile loaded rectangular waveguide is demonstrated in Fig. 3(c) for an inhomogeneous dielectric profile in the cross section. The radius of the circle is denoted as r_1 and the dimensions of the waveguide in the cross-section are denoted as a and b. The refractive index of the core (dielectric profile) is greater than that of the cladding (air). The results of the solution in this case will demonstrate for r_1 = 0.5 mm and for a=b=2 cm. Let us assume that the center of the circle located at the point (a/2, b/2), as shown in Fig. 3(c).

Figures 7(a)-(b) show the results of the output power density (S_{av}) as functions of the step's angle (δ_p=1) and the radius of the cylinder (R=0.5 m). The other parameters are: ζ = 15 cm, a=b= 2 cm, r_1 = 0.5 mm, and λ = 3.75 cm. The output fields are dependent on the input wave profile (TE_{10} mode) and the circular dielectric profile of the rectangular cross section (Fig. 3(c)). Fig. 7(c) shows the output amplitude and the Gaussian shape of the central peak in the same cross section of Figs. 7(a-b), where y=b/2 = 1 cm, and for five values of ϵ_r =2, 5, 6, 8, and 10, respectively. By changing the value of the parameter ϵ_r of the core in the cross section (Fig. 3(c)) with regard to the cladding (air) from 2 to 10, the output transverse profile of the power density (S_{av}) is changed. For small values of ϵ_r, the half-sine (TE_{10}) shape of the output power density appears, with a little influence of the Gaussian shape in the center of the output profile.

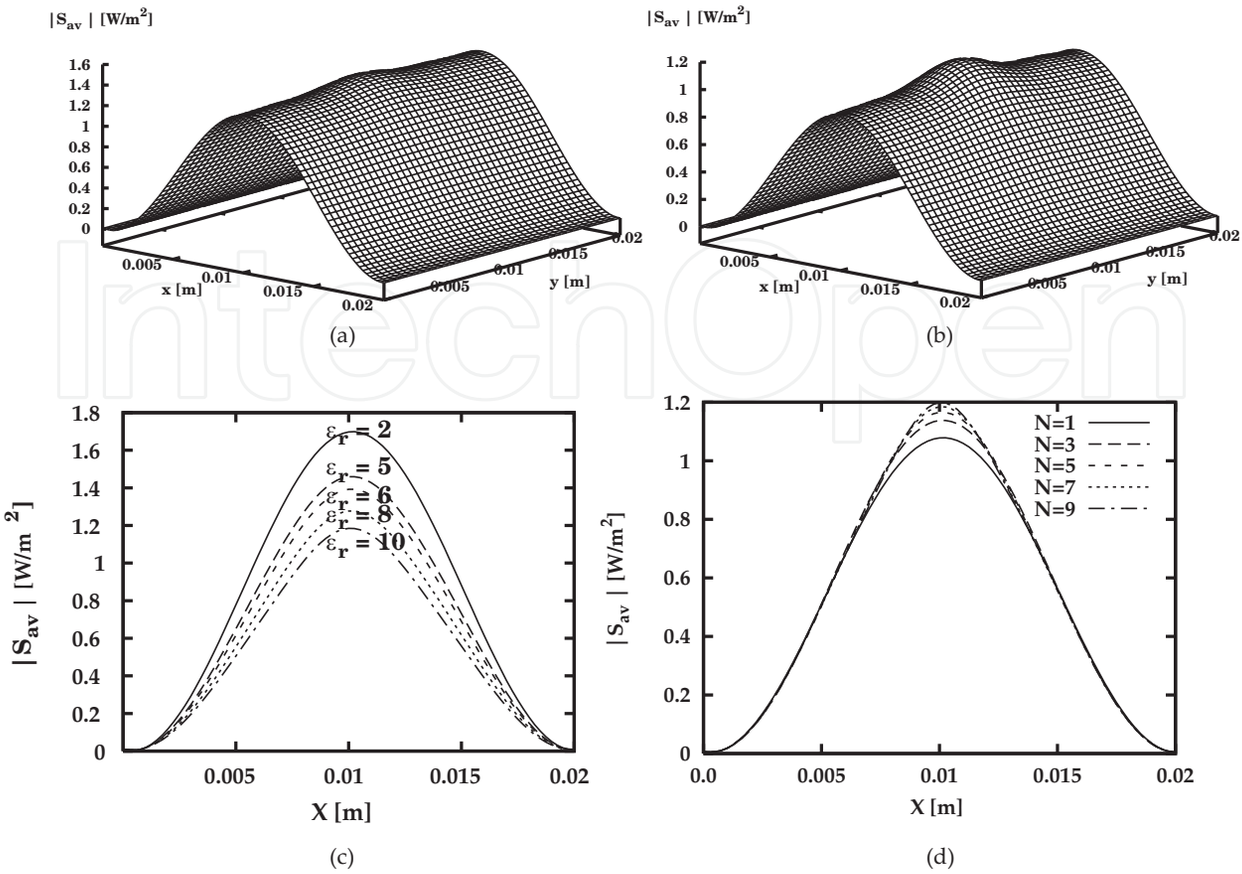

Figure 7. The results of the output power density as functions of the step's angle (δ_p= 1) and the radius of the cylinder (R=0.5 m), where ζ= 15 cm, a=b= 2 cm, r_1 = 0.5 mm, λ = 3.75 cm: (a). ϵ_r = 6; (b). ϵ_r = 10. (c). The output amplitude and the Gaussian shape of the central peak in the same cross section where y=b/2 = 1 cm, and for different values of ϵ_r. (d). The output profile for N=1, 3, 5, 7 and 9, where ϵ_r = 10.

On the other hand, for large values of ϵ_r (e.g., ϵ_r=10) the Gaussian shape of the output power density appears in the center of the output profile (Fig. 7(b)), with a little influence of the half-sine (TE_{10}) shape in the center of the output profile. By increasing only the parameter ϵ_r from 2 to 10, the result of the output power density shows a Gaussian shape and the amplitude of the output power density is changed from 1.6 W/m^2 to 1 W/m^2, as shown in Fig. 7(c). In this case, the output Gaussian profile increases with increasing the value of ϵ_r. These examples demonstrate the influence of the dielectric profile for an inhomogeneous cross section, for arbitrary step's angle and the radius of the cylinder of the helical waveguide. Figure 7(d) shows an example for the output profiles with ϵ_r = 10, and for the same other parameters of Figs. 7(a)-(c). The output results are demonstrated for every order (N=1, 3, 5, 7, and 9). By increasing only the parameter of the order from N=1 to N=9, then the output profile approaches to the final output profile.

The other main contributions of the proposed methods are demonstrated in Fig. 8(a) and in Fig. 8(b), in order to understand the influence of the step's angle (δ_p) and the radius of the cylinder (R) on the output power transmission, for helical waveguide with a circular cross section (Fig. 3(a)) and with a rectangular cross section (Fig. (3(c)), respectively.

Figure 8(a) shows the influence of the step's angle (δ_p) and the radius of the cylinder (R) on the output power transmission for helical waveguide with a circular cross section (Fig. 3(a)). Six results are demonstrated for six values of δ_p (δ_p =0.0, 0.4, 0.7, 0.8, 0.9, 1.0), where ζ = 4 m, a=1 mm, w_0 = 0.06 mm, n_d =2.2 and $n_{(Ag)} = 13.5 - j75.3$. Figure 8(b) shows the influence of the step's angle (δ_p) and the radius of the cylinder (R) on the output power transmission for helical waveguide with a rectangular cross section with a circular dielectric profile (Fig. 3(c)). The output fields are dependent on the input wave profile (TE_{10} mode) and the dielectric profile (Fig. 3(c). Six results are demonstrated for six values of δ_p (δ_p =0, 0.4, 0.7, 0.8, 0.9, 1.0), where ζ = 15 cm, a=b=2 cm, r_1 = 0.5 mm, λ = 3.75 cm, and ϵ_r = 10. For an arbitrary value of R, the output power transmission is large for large values of δ_p and decreases with decreasing the value of δ_p. On the other hand, for an arbitrary value of δ_p, the output power transmission is large for large values of R and decreases with decreasing the value of R. For small values of the step's angle, the radius of curvature of the helix can be approximated by the radius of the cylinder (R). In this case, the output power transmission is large for small values of the bending (1/R), and decreases with increasing the bending. Thus, these two different methods can be a useful tool to find the parameters (δ_p and R) which will give us the improved results (output power transmission) of the curved waveguide in the cases of space curved waveguides.

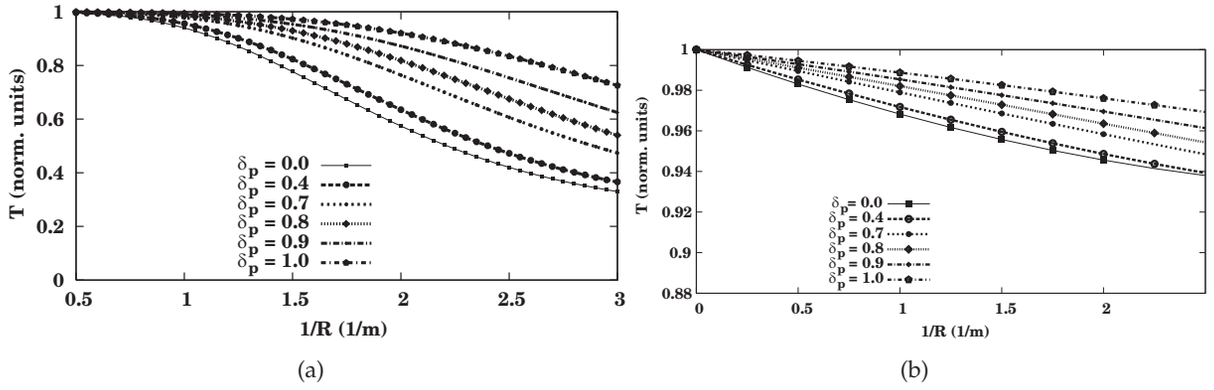

Figure 8. The results of the output power transmission of the helical waveguide as a function of 1/R, where R is the radius of the cylinder. Six results are demonstrated for six values of δ_p (δ_p =0.0, 0.4, 0.7, 0.8, 0.9, 1.0) (a) for circular cross section (Fig. 3(a)), where ζ = 4 m, a=1 mm, w_0 = 0.06 mm, n_d =2.2, and $n_{(Ag)} = 13.5 - j75.3$. (b) for a rectangular cross section with a circular dielectric profile (Fig. 3(c)), where a=20 mm, b=20 mm, r_1 = 0.5 mm, λ = 3.75 cm, and ϵ_r = 10.

5. Conclusions

Two improved methods have been presented for the propagation of EM fields along a helical dielectric waveguide with a circular cross section and a rectangular cross section. The two different methods employ helical coordinates (and not cylindrical coordinates, such as in the methods that considered the bending as a perturbation), and the calculations are based on using Laplace and Fourier transforms. The output fields are computed by the inverse Laplace and Fourier transforms. An example of the circular cross section of the helical waveguide is shown in Fig. 3(a). An example of the rectangular dielectric slab of the helical waveguide is

shown in Fig. 3(b), and an example of the rectangular cross section with a circular dielectric profile of the helical waveguide is shown in Fig. 3(c).

The results of the output transverse components of the fields and the output power density ($|S_{av}|$) (e.g., Fig. 4(a)) for the circular cross section (Fig. 3(a)) show the behavior of the solutions for the TEM_{00} mode in excitation, for the straight waveguide. The result of the output power density (Fig. 4(a)) is compared also to the result of published experimental data [30] as shown also in Fig. 4(b). This comparison shows good agreement (a Gaussian shape) as expected, except for the secondary small propagation mode. The experimental result (Fig. 4(b)) is affected by the additional parameters (e.g., the roughness of the internal wall of the waveguide) which are not taken theoretically into account.

The toroidal dielectric waveguide is demonstrated in Fig. 4(c), and the experimental result is demonstrated in Fig. 4(d). This experimental result was obtained from the measurements of the transmitted CO_2 laser radiation (λ=10.6 μm) propagation through a hollow tube covered on the bore wall with silver and silver-iodide layers (Fig. 3(a)), where the initial diameter (ID) is 1 mm (namely, small bore size). The output modal profile is greatly affected by the bending, and the theoretical and experimental results (Figs. 4(c)-4(d)) show that in addition to the main propagation mode, several other secondary modes and asymmetric output shape appear. The amplitude of the output power density ($|S_{av}|$) is small as the bending radius (R) is small, and the shape is far from a Gaussian shape. This result agrees with the experimental results, but not for all the propagation modes. The experimental result (Fig. 4(d)) is affected by the bending and additional parameters (e.g., the roughness of the internal wall of the waveguide) which are not taken theoretically into account. In both theoretical and experimental results (Figs. 4(c)-4(d)) the shapes of the output power density for the curved waveguide are not symmetric. Fig. 5(a) shows that in addition to the main propagation mode, several other secondary modes appear, where δ_p = 0.4 and R=0.7 m. By increasing only the step's angle, the amplitude of the output power density is greater and also the output shape is changed (Fig. 5(b)).

Figure 6(a) shows the comparison between the theoretical model with the known solution[22] for the rectangular dielectric slab (Fig. 3(b)), for every order (N=1, 3, 5, 7, and 9), where the order N determines the accuracy of the solution. The comparison has shown good agreement. Note that we have two ways to compare between the results of our mode model with the other methods. The first way is to compare between the results of the output fields for every order (N=1, 3, 5, 7, and 9) with the final solution of the known method. The second way is to compare between the results of the output fields (according to our model) for every two orders (N=1,3, N=3,5, N=5,7, and N=7,9), until our numerical solution is well converged. This way is efficient in the cases that we have complicated problems that we cannot compare with the final solution of the known method.

Figures 7(a)-(b) show the results of the output power density (S_{av}) as functions of the step's angle (δ_p=1) and the radius of the cylinder (R=0.5 m). The output fields are dependent on the input wave profile (TE_{10} mode) and the circular dielectric profile of the rectangular cross section (Fig. 3(c)). For small values of ϵ_r, the half-sine (TE_{10}) shape of the output power density appears, with a little influence of the Gaussian shape in the center of the output profile. On the other hand, for large values of ϵ_r (e.g., ϵ_r=10) the Gaussian shape of the output power

density appears in the center of the output profile (Fig. 7(b)), with a little influence of the half-sine (TE_{10}) shape in the center of the output profile. By increasing only the parameter ϵ_r from 2 to 10, the result of the output power density shows a Gaussian shape and the amplitude of the output power density is changed, as shown in Fig. 7(c). In this case, the output Gaussian profile increases with increasing the value of ϵ_r. These examples demonstrate the influence of the dielectric profile for an inhomogeneous cross section, for arbitrary step's angle and the radius of the cylinder of the helical waveguide. Figure 7(d) shows an example for the output profiles with ϵ_r = 10. The output results are demonstrated for every order (N=1, 3, 5, 7, and 9). By increasing only the parameter of the order from N=1 to N=9, then the output profile approaches to the final output profile.

The other main contributions of the proposed methods are demonstrated in Fig. 8(a) and in Fig. 8(b), in order to understand the influence of the step's angle (δ_p) and the radius of the cylinder (R) on the output power transmission, for helical waveguide with a circular cross section (Fig. 3(a)) and with a rectangular cross section (Fig. 3(c)), respectively. Six results are demonstrated for six values of δ_p (δ_p =0.0, 0.4, 0.7, 0.8, 0.9, 1.0), in all case. For an arbitrary value of R, the output power transmission is large for large values of δ_p and decreases with decreasing the the value of δ_p. On the other hand, for an arbitrary value of δ_p, the output power transmission is large for large values of R and decreases with decreasing the value of R. For small values of the step's angle, the radius of curvature of the helix can be approximated by the radius of the cylinder (R). In this case, the output power transmission is large for small values of the bending (1/R), and decreases with increasing the bending. Thus, these two different methods can be a useful tool to find the parameters (δ_p and R) which will give us the improved results (output power transmission) of the curved waveguide in the cases of space curved waveguides.

The output power transmission and the output power density are improved according to the two proposed methods by increasing the step's angle or the radius of the cylinder of the helix, especially in the cases of space curved waveguides. These methods can be a useful tool to improve the output results in all the cases of the hollow helical waveguides in medical and industrial regimes (by the first method) and in the microwave and millimeter-wave regimes (by the second method), for the diffused optical waveguides in integrated optics.

Author details

Z. Menachem and S. Tapuchi
Department of Electrical Engineering, SCE-Shamoon College of Engineering, Israel

6. References

[1] Harrington J.A, Matsuura Y (1995) Review of hollow waveguide technology, *SPIE*, 2396.
[2] Harrington J.A, Harris D.M, Katzir A (1995) *Biomedical Optoelectronic Instrumentation*, pp. 4-14.
[3] Harrington J.A (2000) A review of IR transmitting, hollow waveguides, *Fiber and Integrated Optics*, 19, pp. 211-228.

[4] Marcatili E.A.J, Schmeltzer R.A (1964) Hollow metallic and dielectric waveguides for long distance optical transmission and lasers, *Bell Syst. Tech. J.*, 43, pp. 1783-1809.
[5] Marhic M.E (1981) Mode-coupling analysis of bending losses in IR metallic waveguides, *Appl. Opt.*, 20, pp. 3436-3441.
[6] Miyagi M, Harada K, Kawakami S (1984) Wave propagation and attenuation in the general class of circular hollow waveguides with uniform curvature, *IEEE Trans. Microwave Theory Tech.*, 32, pp. 513-521.
[7] Croitoru N, Goldenberg E, Mendlovic D, Ruschin S, Shamir N (1986) Infrared chalcogenide tube waveguides, *SPIE*, 618, pp. 140-145.
[8] Melloni A, Carniel F, Costa R, Martinelli M (2001) Determination of bend mode characteristics in dielectric waveguides, *J. Lightwave Technol.*, 19, pp. 571-577.
[9] Bienstman P, Roelens M, Vanwolleghem M, Baets R (2002) Calculation of bending losses in dielectric waveguides using eigenmode expansion and perfectly matched layers, *IEEE Photon. Technol. Lett.*, 14, pp. 164-166.
[10] Mendlovic D, Goldenberg E, Ruschin S, Dror J, Croitoru N (1989) Ray model for transmission of metallic-dielectric hollow bent cylindrical waveguides, *Appl. Opt.*, 28, pp. 708-712.
[11] Morhaim O, Mendlovic D, Gannot I, Dror J, Croitoru N (1991) Ray model for transmission of infrared radiation through multibent cylindrical waveguides, *Opt. Eng.*, 30, pp. 1886-1891.
[12] Kark K.W (1991) Perturbation analysis of electromagnetic eigenmodes in toroidal waveguides, *IEEE Trans. Microwave Theory Tech.*, 39, pp. 631-637.
[13] Lewin L, Chang D.C, Kuester E.F (1977) *Electromagnetic Waves and Curved Structures*, Peter Peregrinus Ltd., London, Chap. 6, pp. 58-68.
[14] Cochran J.A, Pecina R.G (1966) Mode propagation in continuously curved waveguides, *Radio Science*, vol. 1 (new series), No. 6, pp. 679-696.
[15] Carle P.L (1987) New accurate and simple equivalent circuit for circular E-plane bends in rectangular waveguide, *Electronics Letters*, vol. 23, No. 10, pp. 531-532.
[16] Weisshaar A, Goodnick S.M, Tripathi V.K (1992) A rigorous and efficient method of moments solution for curved waveguide bends, *IEEE Trans. Microwave Theory Tech.*, vol. MTT-40, No. 12, pp. 2200-2206.
[17] Cornet P, Duss'eaux R, Chandezon J (1999) Wave propagation in curved waveguides of rectangular cross section, *IEEE Trans. Microwave Theory Tech.*, vol. MTT-47, pp. 965-972.
[18] Menachem Z (2003) Wave propagation in a curved waveguide with arbitrary dielectric transverse profiles, *Journal of Electromagnetic Waves and Applications*, 17, No. 10, pp. 1423-1424, and *Progress In Electromagnetics Research, PIER*, 42, pp. 173-192.
[19] Menachem Z, Croitoru N, Aboudi J (2002) Improved mode model for infrared wave propagation in a toroidal dielectric waveguide and applications, *Opt. Eng.*, 41, pp. 2169-2180.
[20] Menachem Z, and Mond M (2006) Infrared wave propagation in a helical waveguide with inhomogeneous cross section and applications, *Progress In Electromagnetics Research, PIER* 61, pp. 159-192.
[21] Menachem Z, Haridim M (2009) Propagation in a helical waveguide with inhomogeneous dielectric profiles in rectangular cross section, *Progress In Electromagnetics Research B*, 16, pp. 155-188.

[22] Collin R.E (1996) Foundation for microwave engineering, New York: McGraw-Hill.
[23] Yariv A (1985) *Optical Electronics*, 3rt edition, Holt-Saunders Int. Editions.
[24] Baden Fuller A.J (1969) *Microwaves*, Pergamon Press, A. Wheaton and Co. Ltd, Oxford, Chap. 5, pp. 118-120.
[25] Olver F.W.J (1960) *Royal Society Mathematical Tables, Zeros and Associated Values*, University Press Cambridge, pp. 2-30.
[26] Jahnke E, Emde F (1945) *Tables of Functions with Formulae and Curves*, Dover Publications, New York, Chap. 8, 166.
[27] Salzer H.E (1955) Orthogonal polynomials arising in the numerical evaluation of inverse Laplace transforms, *Math. Tables and Other Aids to Comut.*, Vol. 9, pp. 164-177.
[28] Salzer H.E (1961) Additional formulas and tables for orthogonal polynomials originating from inversion integrals, *J. Math. Phys.*, Vol. 39, pp. 72-86.
[29] The Numerical Algorithms Group (NAG) Ltd., Wilkinson House, Oxford, U.K..
[30] Croitoru N, Inberg A, Oksman M, Ben-David M (1997) Hollow silica, metal and plastic waveguides for hard tissue medical applications, *SPIE*, 2977, pp. 30-35.